

Research Paper

# Decomposing Infrared Luminosity Functions into Star-Forming and AGN Components using CIGALE

Daniel J. Lyon<sup>1</sup>, Michael J. Cowley<sup>1,2</sup>, Oliver Pye<sup>1</sup>, and Andrew M. Hopkins<sup>3</sup>

<sup>1</sup>School of Chemistry and Physics, 2 George St, Queensland University of Technology, Brisbane, QLD 4000, Australia

<sup>2</sup>Centre for Astrophysics, University of Southern Queensland, West Street, Toowoomba, QLD 4350, Australia

<sup>3</sup>School of Mathematical and Physical Sciences, 12 Wally's Walk, Macquarie University, NSW 2109, Australia

## Abstract

This study presents a comprehensive analysis of the infrared (IR) luminosity functions (LF) of star-forming (SF) galaxies and active galactic nuclei (AGN) using data from the ZFOURGE survey. We employ CIGALE to decompose the spectral energy distribution (SED) of galaxies into SF and AGN components to investigate the co-evolution of these processes at higher redshifts and fainter luminosities. Our CIGALE-derived SF and AGN LFs are generally consistent with previous studies, with an enhancement at the faint end of the AGN LFs. We attribute this to CIGALE's capability to recover low-luminosity AGN more accurately, which may be underrepresented in other works. As anticipated, the CIGALE SF LFs are best fit with a Schechter function, whereas the AGN LFs align more closely with a Saunders function. We find evidence for a significant evolutionary epoch for AGN activity at  $z \approx 1$ , comparable to the peak of cosmic star formation at  $z \approx 2$ , which we also recover well. Based on our results, the gas supply in the early universe favoured the formation of brighter star-forming galaxies until  $z = 2$ , below which the gas for SF becomes increasingly exhausted. Conversely, AGN activity peaked earlier and declined more slowly until  $z \approx 1$ , suggesting a possible feedback scenario in which 2.5 – 3 Gyrs offset the evolution of SF and AGN activity.

**Keywords:** galaxies: luminosity function, mass function; cosmology: observations; infrared: galaxies; galaxies: evolution

(Received xx xx xxxx; revised xx xx xxxx; accepted xx xx xxxx)

## 1. Introduction

The distribution of galaxies and their luminosities have previously derived powerful constraints on galaxy evolution (Binggeli et al. 1988; Benson et al. 2003; Rodighiero et al. 2010; Gruppioni et al. 2013). One of the direct ways of measuring the distribution of galaxies is with the luminosity function (Schechter 1976; Saunders et al. 1990). Luminosity functions (LFs) are statistical distributions that describe the spatial density of astronomical objects and are a fundamental tool for quantifying their evolution across cosmic time scales (Dai et al. 2009; Han et al. 2012; Wylezalek et al. 2014). The use of LFs in galaxy evolution studies has uncovered a wealth of information revealing the intricate processes governing star formation (SF), galaxy mergers, and the growth of supermassive black holes (SMBH,  $M_{BH} > 10^6 M_{\odot}$ ) across cosmic time (Caputi et al. 2007; Hopkins et al. 2007; Magnelli et al. 2013; Delvecchio et al. 2014; Hernán-Caballero et al. 2015). Specifically, many such studies find a strong correlation between the activity of the central SMBH and the star formation rate (SFR) (Hopkins et al. 2008; Merloni & Heinz 2008).

Active galactic nuclei (AGN) are actively accreting SMBHs, whereby massive quantities of gas and dust power their growth (Hopkins et al. 2008; Han et al. 2012; Toba et al. 2013; Brown et al. 2019). It is widely accepted that most galaxies, particularly those with significant bulges, host a SMBH at their centre

(Gruppioni et al. 2011; Han et al. 2012; Brown et al. 2019). While not all central SMBHs are currently active, such as Sagittarius A\* at the centre of our own Milky Way (Event Horizon Telescope Collaboration et al. 2022), most galaxies have likely experienced the influence of an AGN at some point in their history (Gruppioni et al. 2011). SF in galaxies similarly requires an extensive reservoir of cool gas to operate (Schawinski et al. 2007; Cicone et al. 2014). The same interstellar material that powers SF can also fuel AGN growth, leading to an inherent link between these two processes (Hopkins et al. 2008; Brown et al. 2019). This connection has fuelled an ongoing debate over whether AGN activity enhances SF by triggering gas inflows or diminishes it through feedback mechanisms that deplete gas reservoirs (Grazian et al. 2015; Fiore et al. 2017).

Understanding the role of AGN in galaxy evolution is essential, as these processes regulate the growth of the SMBH and the host galaxy's development. Studies have shown that the most luminous AGN are often preceded by periods of intense SF (Kauffmann et al. 2003; Hopkins et al. 2008; Hopkins & Quataert 2010) suggesting a co-evolutionary relationship. Some of this activity is seen as AGN-driven outflow winds that can expel the interstellar medium (ISM) from the galaxy (Schawinski et al. 2007; Cicone et al. 2014; Fiore et al. 2017), thereby starving the galaxy of the cold gas needed for both SF and AGN fueling, ultimately shutting down both processes (Hopkins & Quataert 2010). However, Silk (2013) suggested that AGN-driven winds may, under certain conditions, compress gas and dust, thereby enhancing SF. This scenario aligns with findings from Cowley et al. (2016), which

**Author for correspondence:** Daniel Lyon, Email: daniellyon31@gmail.com

**Cite this article:** Author1 C and Author2 C, an open-source python tool for simulations of source recovery and completeness in galaxy surveys. *Publications of the Astronomical Society of Australia* 00, 1–12. <https://doi.org/10.1017/pasa.xxxx.xx>

indicate that AGN-dominated systems tend to have higher specific star formation rates, suggesting that SF and AGN activity can co-exist in certain environments.

Both SF and AGN activity releases an enormous amount of energy across the entire electromagnetic spectrum, from radio waves to gamma rays (Ho 1999; Huang *et al.* 2007; Silva *et al.* 2011; Gruppioni *et al.* 2011). LFs at various wavelengths have been used to place powerful constraints on evolutionary models, as seen in Aird *et al.* (2015); Alqasim & Page (2023) (X-ray), Yuan *et al.* (2018) (Radio), Page *et al.* (2021) (UV), and Cool *et al.* (2012) (optical). However, the properties of Infrared (IR) light make it the ideal regime for studying SF and AGN LFs as both processes are often dusty and obscured (optically thick) (Wu *et al.* 2011; Han *et al.* 2012). Dust extinction absorbs the outgoing X-ray, optical, and UV wavelengths and re-emits the radiation in the IR domain (Fu *et al.* 2010; Toba *et al.* 2013; O'Connor *et al.* 2016; Symeonidis & Page 2021). AGN activity is closely correlated with IR luminosity because the IR emission often traces dust heated by AGN (Kauffmann *et al.* 2003; Wu *et al.* 2011; Symeonidis & Page 2019, 2021). However, this can create a bias against detecting faint AGN. This bias may also explain why AGN feedback appears to be more prevalent at lower redshifts (Katsianis *et al.* 2017; Pouliaxis *et al.* 2020). The relationship between IR luminosity and SFR is complex (Symeonidis & Page 2021) and becomes weaker at brighter luminosities and higher redshifts, where AGN contribution to the IR emission increases (Wu *et al.* 2011).

Most studies focus on galaxy or SF LFs, which trace the evolution of galaxies (Tempel 2011; Cool *et al.* 2012), but often neglect the co-evolution with AGN (Fotopoulou *et al.* 2016; Symeonidis & Page 2021; Finkelstein & Bagley 2022) even though galaxies are known to be significantly influenced by this relationship (Hopkins *et al.* 2008; Fiore *et al.* 2017). The population of obscured, dusty IR AGN and SFGs play a crucial role in constraining galaxy evolution models (Gruppioni *et al.* 2011). Analysing the SF and AGN LFs is paramount to understanding the complex processes driving galaxy evolution. SF LFs allow us to quantify the cosmic star formation rate history and the star-formation rate density. At the same time, the AGN LF provides insight into gas reservoirs not utilised by SF, particularly in the context of feedback mechanisms.

Since SF and AGN activity are so tightly coupled, distinguishing between the two components can be challenging. Traditional methods of selecting AGN, such as colour-colour diagnostics (Lacy *et al.* 2004), X-ray dominated (Szokoly *et al.* 2004), and radio-dominated (Rees *et al.* 2016) approaches, often overlook faint AGN due to biases inherent in their selection criteria (Thorne *et al.* 2022). This limitation highlights the need for more refined methods of identifying AGN to better constrain galaxy evolution. In this paper, we use Code Investigating Galaxy Emission (CIGALE, Burgarella *et al.* 2005; Noll *et al.* 2009; Boquien *et al.* 2019) to decompose the IR Spectral Energy Distribution (SED) of ZFOURGE galaxies (Straatman *et al.* 2016) to generate and analyse both the SF and AGN LFs. Incorporating SED decomposition is crucial for interpreting the co-evolution of galaxies with AGN. SEDs characterise many ongoing processes such as the SF and AGN components, as well as dust attenuation and gas heating (Ho 1999; Huang *et al.* 2007; Silva *et al.* 2011; Gruppioni *et al.* 2011). We focus on the SF and AGN components to probe galaxy evolution directly. SED decomposition will allow us to independently quantify SF and AGN evolution while minimising the bias against faint AGN.

To achieve this, we leverage data from the ZFOURGE survey, which probes galaxies at higher redshifts and fainter luminosities,

allowing for more precise constraints on the evolution of the SFR and AGN activity across cosmic time. By decomposing the SED of each galaxy, we can disentangle the contributions of SF and AGN to galaxy evolution, providing a clearer picture of how these processes interact. Our approach minimises biases against faint AGN and improves the accuracy of the derived LFs. In section 2, we introduce the ZFOURGE Survey and an overview of our data generation and reduction. In section 3, we overview CIGALE and how we performed the SED decomposition process to disentangle SF and AGN luminosities. In section 4, we provide a brief outline of how we calculate the LFs, the errors, and the functional fitting process. Finally, in section 5, we discuss the results of our LFs, the parameter evolution, luminosity density, and luminosity class evolution in the broader context of galaxy co-evolution with AGN and SFR. Throughout this paper we adopt a cosmology of  $H_0 = 70$  km s<sup>-1</sup> Mpc<sup>-1</sup>,  $\Omega_m = 0.7$ , and  $\Omega_\Lambda = 0.3$ .

## 2. The ZFOURGE Survey

### 2.1. Overview

This study utilises the 2017 release<sup>a</sup> of the ZFOURGE survey (Straatman *et al.* 2016), which offers a unique combination of depth and wavelength coverage essential for probing high-redshift galaxies and constructing accurate LFs. ZFOURGE consists of approximately 70,000 galaxies at redshifts greater than 0.1 covering three major 11×11 arcminute fields: the Chandra Deep Field South (CDFs) (Giacconi *et al.* 2002), the field observed by the Cosmic Evolution Survey (COSMOS) (Scoville *et al.* 2007), and the CANDELS Ultra Deep Survey (UDS) (Lawrence *et al.* 2007). These galaxies were observed using the near-infrared FourStar imager (Persson *et al.* 2013) mounted on the 6.5-m Magellan Baade Telescope at the Las Campanas Observatory in Chile.

ZFOURGE employs deep near-infrared imaging with multiple medium-band filters ( $J_1$ ,  $J_2$ ,  $J_3$ ,  $H_l$ ,  $H_s$ ) and a broad-band  $K_s$  filter. The imaging spans 1.0 to 1.8  $\mu\text{m}$  and achieves  $5\sigma$  point-source limiting depths of 26 AB mag in the  $J$  medium-bands and 25 AB mag in the  $H$  and  $K_s$  bands (Spitler *et al.* 2012). These filters yield well-constrained photometric redshifts, particularly effective for sources within the redshift range of 1 to 4 (Spitler *et al.* 2012). ZFOURGE data is supplemented by public data from HST/WFC3 F160W and F125W imaging from the CANDELS survey, Spitzer/Infrared Array Camera (IRAC), and Herschel/Photodetector Array Camera and Spectrometer (PACS). For a detailed description of the data and methodology, refer to Straatman *et al.* (2016).

### 2.2. Sample Selection

To ensure the selection of high-quality galaxies and minimise errors in our analysis, we adopt the ZFOURGE quality flag  $\text{Use}=1$ , as defined by Straatman *et al.* (2016). This flag selects galaxies with reliable photometry and redshift measurements, resulting in a starting sample of 37,647 galaxies. We refine the sample by removing sources with unphysical bolometric luminosities ( $L_{bol} < 0$ ), which reduces the sample to 22,967 galaxies.

#### 2.2.1. ZFOURGE total & Decomposed SF Sample

Next, we use the ZFOURGE AGN catalogues (Cowley *et al.* 2016) to identify and exclude 552 AGN-dominated sources to prevent AGN contamination of the luminosity functions. After excluding

<sup>a</sup>Available for download at [zfourge.tamu.edu](http://zfourge.tamu.edu).

these AGN sources, we apply a redshift cut, restricting the sample to  $0 \leq z \leq 6$  since only 28 galaxies exist at  $z > 6$ . This redshift range enables us to observe the evolution of galaxies during some of the most critical cosmic periods, specifically around  $1 < z < 3$  (Gruppioni et al. 2011; Wylezalek et al. 2014) where galaxy luminosity density peaks (Assef et al. 2011). This sample includes 22,444 galaxies, which we use to construct the ZFOURGE total and CIGALE SF LFs.

To ensure robustness, we calculate the bolometric flux from the bolometric luminosity of each sample and apply an 80% completeness cut. This reduces the impact of noise and observational limits while preserving a large enough sample for LF construction. We also apply a completeness cut that requires the maximum observable volume of each galaxy to extend to the end of the redshift bin. These completeness cuts reduce the final LF sample to 16,154 galaxies.

### 2.2.2. Decomposed AGN Sample

Although AGN-dominated sources are removed from the ZFOURGE galaxy and CIGALE SF sample, they are retained for separate analysis to construct decomposed AGN LFs through SED decomposition. For a comprehensive explanation of the SED decomposition process, please refer to Section 3. For this AGN-specific analysis, we include all sources with a significant AGN fraction ( $\mathcal{F}_{AGN} > 0.1 L_{AGN}/L_{bol}$ ); 12,390 sources. Applying the same luminosity completeness cut and 80% completeness cut to the bolometric flux, the AGN sample is reduced to a final set of 8,800 galaxies spanning  $0 \leq z \leq 6$ . Figure 1 shows the reduced luminosity-redshift distribution of ZFOURGE (top), CIGALE AGN (middle), and CIGALE SF (bottom).

## 3. Decomposing Galaxy SEDs

The public version of the ZFOURGE catalogues has utilised EAZY (Brammer et al. 2008) and FAST (Kriek et al. 2009) for parameterising galaxy properties, primarily focusing on photometric redshifts, stellar masses, and SFRs. However, while effective, these methods provide a more generalised view of galaxy properties without entirely disentangling the contributions from different physical components within each galaxy, such as SF regions and AGN. To address this limitation, we employ the SED fitting software CIGALE (Boquien et al. 2019), which enables the decomposition of observed light from galaxies into distinct components, including SF and AGN activity. This method builds on the work by Cowley et al. (2018), incorporating additional photometric coverage and an updated parameter space to better quantify AGN contributions.

### 3.1. CIGALE Methodology and Parameter Space

CIGALE performs multi-component SED fitting to derive galaxy properties by integrating our photometry from  $0.2 \mu\text{m}$  to  $160 \mu\text{m}$  across the CDFS field and up to  $24 \mu\text{m}$  for COSMOS and UDS. This broader wavelength coverage allows for a more complete and precise decomposition of galaxy light into SF and AGN components. The decomposition uses a range of parameter values (see Table 1), allowing for flexible modelling of star formation histories (SFH), dust attenuation, AGN torus contributions, and other factors. We also incorporate the SKIRTOR AGN torus model (Stalevski et al. 2016), which better handles clumpy dust distributions and polar dust extinction, providing an accurate characterisation of AGN emission.

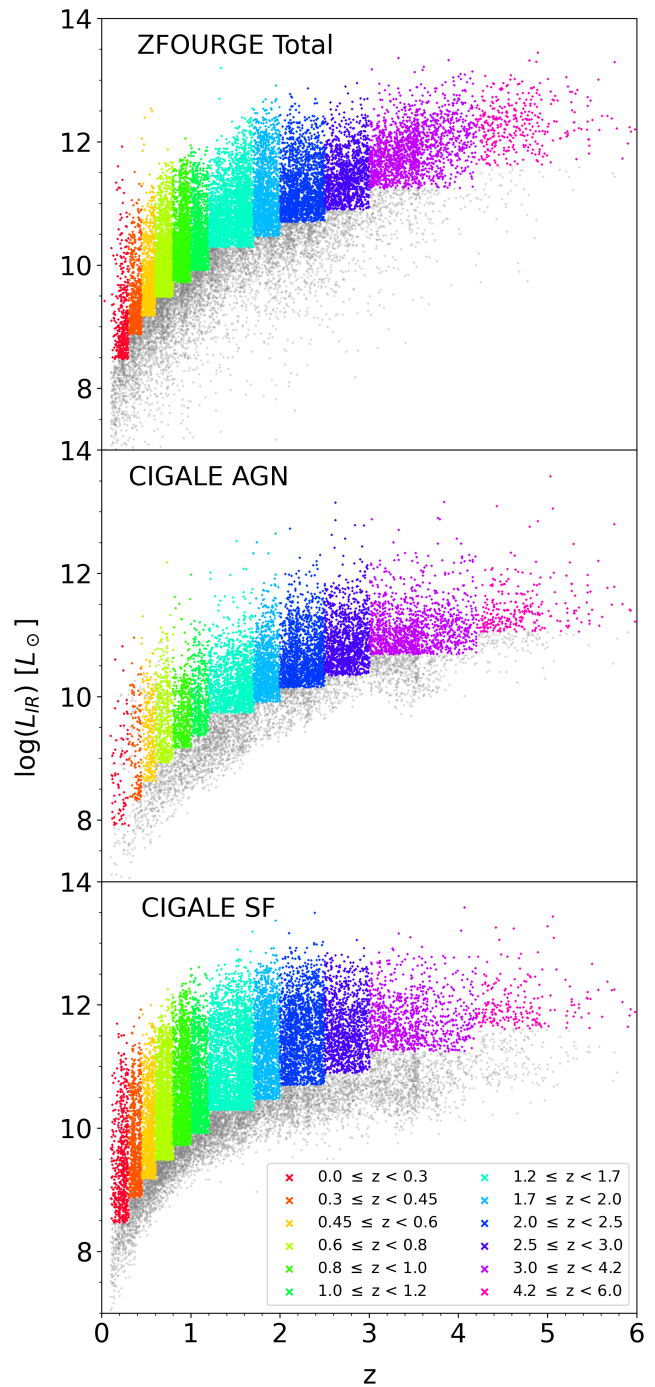


**Figure 1:** Luminosity-redshift distributions of (top) the ZFOURGE bolometric  $8 - 1000 \mu\text{m}$  luminosity, (middle) the CIGALE AGN luminosity, and (bottom) the CIGALE SF luminosity. Sources are coloured by redshift bin or coloured grey if removed as described in section 2.2

### 3.2. Bolometric IR Luminosity Derivation

Understanding the total IR energy output of galaxies is essential for tracing both SF and AGN activity, particularly in dusty environments where much of the energy is re-emitted in the IR (Fu et al. 2010). By estimating the bolometric IR luminosity, we can

gain insights into the contribution of these processes across cosmic time.

For the ZFOURGE total LF sample, we adopted the approach in Straatman *et al.* (2016) where the averaged Wuyts *et al.* (2008) template was fit to the 24–160  $\mu\text{m}$  photometry to estimate the total bolometric IR luminosity. This method provides a robust measure of the IR emission for purely star-forming galaxies without AGN contamination.

For the Decomposed SF and AGN LF samples, we derive luminosities through a different approach. CIGALE performs SED decomposition on the entire galaxy emission, using its integrated models to separate the total luminosity into distinct stellar, dust, and AGN components. The stellar and dust luminosities are combined to form the SF component, while the AGN component is derived directly from CIGALE’s emission modelling. These distinct approaches are subsequently used to construct the IR luminosity functions of the two samples.

Figure 2 compares the CIGALE total luminosity to the ZFOURGE total bolometric luminosity ( $L_{\text{bol}}$ ). In the top panel, galaxies are coloured based on their redshift bin. It can be seen that the brightest galaxies are more likely to exist at higher redshifts. In the bottom panel, galaxies are coloured based on the AGN fraction ( $F_{\text{AGN}}$ ) to the total luminosity derived by CIGALE. Galaxies at higher redshift are brighter and more likely to host a powerful AGN.

Table 1. : Parameter space used for SED fitting with CIGALE

Parameter	Model/Values
SFH	Delayed SFH $\tau = 1, 3, 5, 7, 9, 11$ Gyr
Age	0.5, 1, 3, 5, 7, 9, 11 Gyr
Burst Fraction	0.0, 0.01, 0.05, 0.1, 0.15, 0.2, 0.3
SSP	Bruzual & Charlot (2003)
IMF	Chabrier (2003)
Metallicity	Fixed at 0.02
Nebular	Inoue (2011)
Dust Atten.	Calzetti <i>et al.</i> (2000) $E_{(B-V)} = 0.01, 0.05, 0.1, 0.5, 1.0, 1.5$
Dust Emission	Dale <i>et al.</i> (2014) $\alpha = 1.0, 1.5, 2.0, 2.5, 3.0$
AGN Model	SKIRTOR (Stalevski <i>et al.</i> 2012, 2016)
Torus Inclination	$30^\circ, 70^\circ$
AGN Fraction	0.0, 0.01, 0.1 – 0.9 (steps of 0.1), 0.99
Polar Extinction	SMC $E(B-V) = 0.0, 0.03, 0.1, 0.2, 0.4, 0.6, 1.0, 1.8$

### 3.3. Robustness Tests with Mock Analysis

To ensure the reliability of the decomposition process, particularly for faint AGN, we performed a series of robustness tests using CIGALE’s built-in mock analysis. These tests evaluate the software’s ability to accurately decompose AGN and SF contributions across various redshifts and luminosities, specifically focusing on galaxies with low bolometric luminosities. By comparing the input and recovered AGN luminosities from the analysis, we confirmed

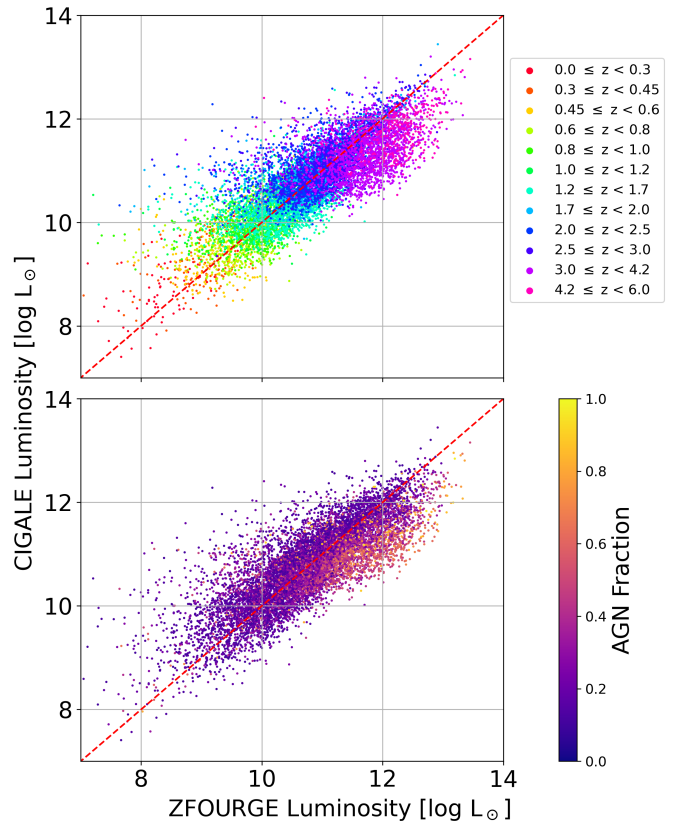


Figure 2: ZFOURGE bolometric 8–1000 $\mu\text{m}$  IR luminosity compared to CIGALE total luminosity. Top: Sources coloured by redshift bin. Bottom: sources coloured by AGN fraction ( $F_{\text{AGN}}$ ). AGN fraction increases with redshift. At  $z \geq 3$ , the average AGN fraction is greater than 30%.

that our parameter space and methodology are robust, particularly in detecting faint AGN. The mock analysis demonstrated that AGN luminosity was reliably constrained, with Pearson correlation coefficients (PCCs) ranging from 0.969 to 0.973 across all fields. Most sources lay within 0.5 dex of the 1-to-1 line, with mean residuals between  $-0.02$  and  $0.04$  dex, confirming the robustness of AGN luminosity recovery. These results indicate that our method effectively minimises bias against faint AGN, which are often difficult to detect in traditional analyses.

For a more comprehensive description of the SED decomposition methodology, see Cowley *et al.* (2018). Additionally, refer to the CIGALE software paper (Boquien *et al.* 2019) for detailed information on its decomposition process and parameter optimisation techniques.

## 4. Luminosity Functions

### 4.1. $V_{\text{max}}$

To estimate the LF from our data, we utilise the  $1/V_{\text{max}}$  method (Schmidt 1968). The  $1/V_{\text{max}}$  method is well-suited for surveys like ZFOURGE, as it does not assume any specific shape for the LF and can easily accommodate galaxies observed across varying depths. It accounts for the maximum observable volume of each galaxy and is given by equation 1:

$$\phi(L, z) = \frac{1}{\Delta \log L} \sum_{i=1}^N \frac{1}{V_{\text{max},i}} \quad (1)$$

Where  $V_{max}$  represents the maximum co-moving volume of the  $i$ -th source and  $\Delta \log(L)$  is the width of the luminosity bin. In practice, to observe the evolution of the LF through cosmic time, the maximum observable volume ( $V_{max}$ ) is calculated for each redshift bin where the upper and lower bounds of the redshift bin limit the volume. Additionally, redshift bins are split into luminosity bins to observe the number density evolution across the different classes of luminosity such as LIRGs ( $10^{11} < L_{IR} < 10^{12} L_{\odot}$ ) and ULIRGs ( $L_{IR} > 10^{12} L_{\odot}$ ).  $V_{max}$  of each galaxy is calculated by taking the maximum comoving volume of the redshift bin the galaxy resides in and subtracting the comoving volume at the beginning of the redshift bin (equation 2). We account for the survey area of ZFOURGE (0.1111 degrees<sup>2</sup>), which normalises the volume probed across the sky (41,253 degrees<sup>2</sup>).

$$V_{max,i} = \frac{4}{3} \pi (D_{max}^3 - D_{min}^3) \times \frac{A}{41,253} \quad (2)$$

We calculate the maximum ( $D_{max}$ ) and minimum ( $D_{min}$ ) comoving distances for all sources within each redshift bin using the FlatLambdaCDM model from the Astropy Python package (Astropy Collaboration et al. 2022). These calculations are performed for sources above the luminosity-completeness limits (coloured sources of figure 1). We limit each luminosity bin to a minimum of five sources, or else the luminosity bin is discarded.

Sources with  $D_{max}$  values that do not extend to the end of the redshift bin are removed to avoid bias from sources incompletely sampled within the bin. Different redshift bins have different volumes, and each luminosity bin has a different number density  $\phi$ .  $D_{min}$  and  $D_{max}$  are the comoving distances at the beginning and end of the redshift bin, respectively, for all galaxies. The relative LF number density  $1\sigma$  error values are calculated with:

$$\phi(L, z) = \frac{1}{\Delta \log L} \sqrt{\sum_i \frac{1}{V_{max}^2}} \quad (3)$$

## 4.2. Fitting Functions

We first construct the bolometric IR LF using the ZFOURGE dataset. Then, using CIGALE, we decompose the luminosity into contributions from SF regions and AGN, allowing us to investigate the evolution of these components separately.

To model LFs, one of the most widely used methods is the Schechter function (Schechter 1976). This function is beneficial for describing the LF of galaxies because it can represent observed features, such as a power-law decline at the faint end and an exponential cutoff at the bright end. We employ the Schechter function to model the CIGALE SF LF as both Fu et al. (2010) and Wu et al. (2011) have shown that pure SF LFs fit better with a Schechter function. The Schechter function is mathematically represented by equation 4:

$$\phi(L) = \phi^* \left(\frac{L}{L^*}\right)^{1-\alpha} \exp\left(-\frac{L}{L^*}\right) \quad (4)$$

Where  $\phi(L)$  is the number of galaxies per unit volume (number density),  $\phi^*$  is the characteristic normalisation factor,  $L$  is the bolometric IR (8-1000 $\mu$ m) luminosity,  $L^*$  is the characteristic luminosity, and  $\alpha$  is the faint end slope (Schechter 1976). The Schechter function, however, is not the only commonly used fitting function at mid- and far-IR wavelengths. The bright end slope

of the Schechter function cannot be independently varied to fit a dataset better. We make use of a modified Schechter function known as the Saunders function (Saunders et al. 1990; equation. 5) to fit our ZFOURGE total and CIGALE AGN LFs:

$$\phi(L) = \phi^* \left(\frac{L}{L^*}\right)^{1-\alpha} \exp\left[-\frac{1}{2\sigma^2} \log_{10}^2\left(1 + \frac{L}{L^*}\right)\right] \quad (5)$$

Where the parameters are the same as the Schechter function (equation 4), but with the introduction of  $\sigma$  to vary the bright end slope. Our deep ZFOURGE data probes to fainter luminosities than often seen in the literature (e.g. Rodighiero et al. 2010; Gruppioni et al. 2013), thus better constraining the faint end of the LF. However, as ZFOURGE is designed to probe deeper into the universe, we lack brighter galaxies at lower redshifts.

## 5. Discussion

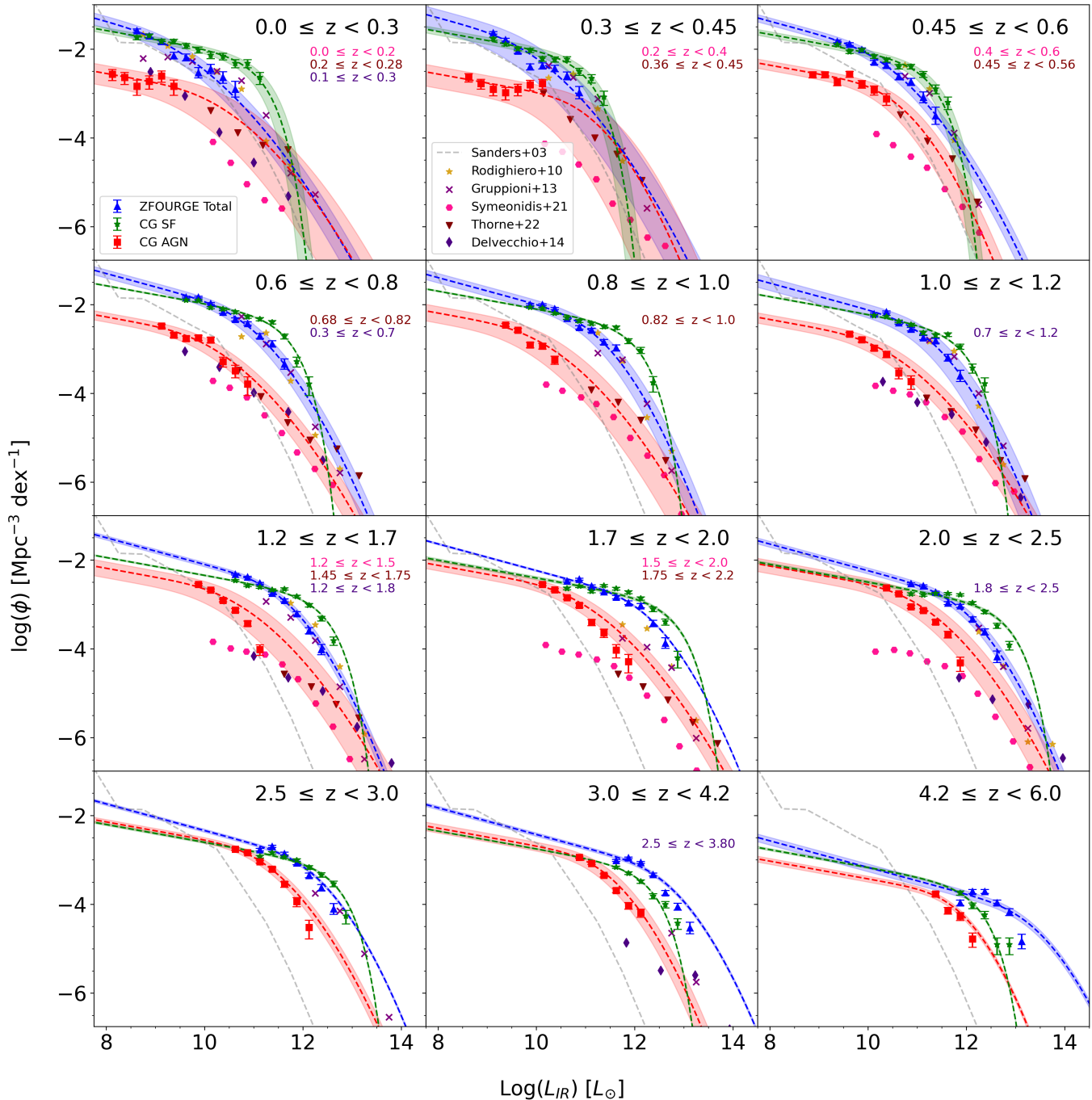
### 5.1. Bolometric IR LF

Figure 3 presents the bolometric IR LFs derived from the ZFOURGE and CIGALE samples. This comparison allows us to explore the evolution of total IR emission and the individual contributions from SF and AGN across twelve redshift bins from  $0 \leq z < 6$ . By comparing the total LF from ZFOURGE with the decomposed SF and AGN LFs from CIGALE, we aim to better understand the distinct roles of SF and AGN activity in galaxy evolution over cosmic time. To model these LFs, we employ `scipy.optimize.curve_fit` (Virtanen et al. 2020) to perform the fitting and calculate  $1\sigma$  relative parameter dispersion errors using `np.sqrt(np.diag(pcov))` from NumPy (Harris et al. 2020).

#### 5.1.1. ZFOURGE Total

Focusing first on the ZFOURGE data, we compare our results with Rodighiero et al. (2010) and Gruppioni et al. (2013). We also compare our results with Huang et al. (2007); Caputi et al. (2007); Fu et al. (2010) but avoid cluttering figure 3 with these disjointed redshift bins from the literature. Across all redshift bins (except the most local), we consistently see that the ZFOURGE number density ( $\phi$ ) values in blue extend much fainter than the rest of the literature, showcasing ZFOURGE's ability to probe to fainter luminosities. However, there remains room to improve the constraints at the faint end of the ZFOURGE LF. Extending the analysis by an additional order of magnitude fainter in each redshift bin would significantly enhance our ability to constrain the faint-end slope.

Our ZFOURGE results agree very well with the literature in all bins except  $1.7 \leq z < 2$  and  $3.0 \leq z < 4.2$ . In these redshift bins, ZFOURGE results show  $\phi$  values  $\approx 0.5$  dex higher across all luminosity bins when compared to the literature (Rodighiero et al. 2010; Gruppioni et al. 2013). We posit that ZFOURGE is detecting fainter sources in these redshift bins than previously observed. From  $1.7 \leq z < 2$ , both Rodighiero et al. (2010) and Gruppioni et al. (2013) show a drop in their faintest luminosity bins, consistent with incompleteness. Gruppioni et al. (2013) sees a decline of  $\approx 0.5 \log(\phi)$  or more in each luminosity bin from  $3.0 \leq z < 4.2$  when compared to their previous redshift bin and is likely to be solely an incompleteness issue given it is their final redshift bin. The fact that both Gruppioni et al. (2013) and Rodighiero et al. (2010) see a drop from  $1.7 \leq z < 2$  is intriguing. This issue does not appear in neighbouring redshift bins or



**Figure 3:** The luminosity functions of major galaxy populations in ZFOURGE and CIGALE calculated using the Vmax method. The dark blue triangles present the ZFOURGE bolometric IR (8-1000 $\mu$ m) LF. The CIGALE SF and AGN LFs are the green stars and red squares, respectively. The blue and red dashed lines show the best fit Saunders function (Saunders et al. 1990) to the ZFOURGE total and CIGALE AGN LF, respectively. The green dashed line shows the best-fit Schechter function (Schechter 1976) to the CIGALE SF LF. The shaded regions represent the  $1\sigma$  functional fit errors. The luminosity completeness limit of each redshift bin is where we stop displaying fainter  $\phi$  values. Where possible, comparable literature results are also shown. The local Sanders et al. (2003) luminosity function is shown across all redshift bins as the grey dashed line. Rodighiero et al. (2010) is shown as gold filled stars from  $0 < z < 2.5$ , Gruppioni et al. (2013) as purple crosses from  $0 < z < 4.2$ , Symeonidis & Page (2021) AGN as pink hexagons, Thorne et al. (2022) AGN as maroon upside-down triangles, Delvecchio et al. (2014) AGN as indigo diamonds. Differing redshift bins are colour-labelled accordingly. Our ZFOURGE total results are consistent with various sources across redshift bins in the literature (Caputi et al. 2007; Huang et al. 2007; Fu et al. 2010)

Table 2. : ZFOURGE bolometric IR (8-1000 $\mu$ m) LF  $\phi$  values.

$\log_{10}(L_{IR}/L_{\odot})$	$0.00 \leq z < 0.30$	$0.30 \leq z < 0.45$	$0.45 \leq z < 0.60$	$0.60 \leq z < 0.80$	$0.80 \leq z < 1.00$	$1.00 \leq z < 1.20$
8.50 – 8.75	$-1.58 \pm 0.04$	-	-	-	-	-
8.75 – 9.00	$-1.70 \pm 0.04$	-	-	-	-	-
9.00 – 9.25	$-1.83 \pm 0.05$	$-1.64 \pm 0.03$	-	-	-	-
9.25 – 9.50	$-2.15 \pm 0.07$	$-1.79 \pm 0.03$	$-1.83 \pm 0.03$	-	-	-
9.50 – 9.75	$-2.19 \pm 0.08$	$-2.05 \pm 0.05$	$-1.89 \pm 0.03$	$-1.83 \pm 0.02$	-	-
9.75 – 10.00	$-2.54 \pm 0.12$	$-2.40 \pm 0.07$	$-2.01 \pm 0.03$	$-1.83 \pm 0.02$	$-2.00 \pm 0.02$	-
10.00 – 10.25	$-2.45 \pm 0.11$	$-2.38 \pm 0.07$	$-2.30 \pm 0.05$	$-1.98 \pm 0.02$	$-2.00 \pm 0.02$	$-2.21 \pm 0.03$
10.25 – 10.50	$-2.64 \pm 0.13$	$-2.44 \pm 0.07$	$-2.37 \pm 0.05$	$-2.17 \pm 0.03$	$-2.09 \pm 0.02$	$-2.17 \pm 0.02$
10.50 – 10.75	$-2.90 \pm 0.18$	$-2.60 \pm 0.09$	$-2.62 \pm 0.07$	$-2.34 \pm 0.04$	$-2.31 \pm 0.03$	$-2.41 \pm 0.03$
10.75 – 11.00	-	$-2.98 \pm 0.14$	$-2.74 \pm 0.08$	$-2.43 \pm 0.04$	$-2.52 \pm 0.04$	$-2.56 \pm 0.04$
11.00 – 11.25	-	-	$-3.09 \pm 0.12$	$-2.71 \pm 0.06$	$-2.58 \pm 0.04$	$-2.75 \pm 0.05$
11.25 – 11.50	-	-	$-3.50 \pm 0.19$	$-2.89 \pm 0.07$	$-2.85 \pm 0.06$	$-2.82 \pm 0.05$
11.50 – 11.75	-	-	-	$-3.34 \pm 0.12$	$-2.98 \pm 0.07$	$-3.20 \pm 0.08$
11.75 – 12.00	-	-	-	-	-	$-3.61 \pm 0.13$
$\log_{10}(L_{IR}/L_{\odot})$	$1.20 \leq z < 1.70$	$1.70 \leq z < 2.00$	$2.00 \leq z < 2.50$	$2.50 \leq z < 3.00$	$3.00 \leq z < 4.20$	$4.20 \leq z < 6.00$
10.50 – 10.75	$-2.33 \pm 0.02$	$-2.47 \pm 0.02$	-	-	-	-
10.75 – 11.00	$-2.39 \pm 0.02$	$-2.43 \pm 0.02$	$-2.54 \pm 0.02$	-	-	-
11.00 – 11.25	$-2.52 \pm 0.02$	$-2.59 \pm 0.03$	$-2.58 \pm 0.02$	$-2.77 \pm 0.03$	-	-
11.25 – 11.50	$-2.75 \pm 0.03$	$-2.71 \pm 0.03$	$-2.73 \pm 0.02$	$-2.70 \pm 0.02$	-	-
11.50 – 11.75	$-2.91 \pm 0.03$	$-2.84 \pm 0.04$	$-2.97 \pm 0.03$	$-2.86 \pm 0.03$	$-3.02 \pm 0.02$	-
11.75 – 12.00	$-3.21 \pm 0.05$	$-2.96 \pm 0.04$	$-3.03 \pm 0.03$	$-3.07 \pm 0.04$	$-2.96 \pm 0.02$	$-3.97 \pm 0.06$
12.00 – 12.25	$-3.59 \pm 0.07$	$-3.03 \pm 0.05$	$-3.33 \pm 0.05$	$-3.35 \pm 0.05$	$-3.06 \pm 0.02$	$-3.71 \pm 0.05$
12.25 – 12.50	$-4.02 \pm 0.12$	$-3.43 \pm 0.07$	$-3.62 \pm 0.07$	$-3.63 \pm 0.07$	$-3.33 \pm 0.03$	$-3.71 \pm 0.04$
12.50 – 12.75	-	$-3.87 \pm 0.12$	$-4.18 \pm 0.13$	$-4.11 \pm 0.12$	$-3.74 \pm 0.05$	$-3.97 \pm 0.06$
12.75 – 13.00	-	-	-	-	$-4.06 \pm 0.08$	$-4.18 \pm 0.08$
13.00 – 13.25	-	-	-	-	$-4.53 \pm 0.13$	$-4.84 \pm 0.16$

**Note:** Luminosity bin  $\phi$  values are centred.

other redshift bins. Rodighiero et al. (2010) utilises multiwavelength Spitzer observations, whereas Gruppioni et al. (2013) uses Herschel/PACS data to estimate the total IR LF. Given that this incompleteness exists across multiple surveys and instruments, it remains to be seen why a drop in the  $1.7 \leq z < 2$  redshift bin exists when neighbouring redshift bins show no sign of incompleteness. Similar can be said about our final redshift bin  $4.2 \leq z < 6.0$  (figure 3). Luminosity bins in this redshift range show a drop along the faint end slop of our LF. Therefore, the redshift bin  $4.2 \leq z < 6.0$  is likely incomplete and should be taken as a lower limit.

### 5.1.2. CIGALE AGN

For the CIGALE AGN, we compare our results with Delvecchio et al. (2014); Symeonidis & Page (2021) and Thorne et al. (2022). Symeonidis & Page (2021) derives their IR AGN  $\phi$  values from the hard X-ray LFs by Aird et al. (2015). Thorne et al. (2022), who performs similar work to this analysis, uses the SED fitting code ProSpect (Leja et al. 2017; Robotham et al. 2020) to decompose the bolometric IR LF and recover the pure AGN component to the LF. We fit the Saunders function in red and  $1\sigma$  uncertainties to our CIGALE decomposed AGN LF. We include Thorne et al. (2022)

AGN in our fitting process as we do not have comparatively bright AGN to constrain the bright end of the LF.

In the first few redshift bins from  $0 \leq z < 0.8$ , our CIGALE AGN LF and the Saunders function fits are generally consistent with the results in the literature. However, the literature LFs tend to flatten considerably at higher redshifts and fainter luminosities. In contrast, our CIGALE AGN LFs do not flatten and instead continue to rise, suggesting that CIGALE SED decomposition is effective in isolating and recovering the AGN contribution to luminosities as faint as  $10^8 L_{\odot}$ . Furthermore, we probe fainter than Thorne et al. (2022) whose faintest luminosity bins are never less than  $10^{10} L_{\odot}$  when accounting for completeness limits. While our CIGALE AGN lacks  $\phi$  values at the brighter end of the LF, necessitating the use of Thorne et al. (2022)  $\phi$  values to constrain our Saunders function fits, CIGALE's ability to extend the LF to such faint luminosities provides crucial insights into the AGN population at higher redshifts.

Because the IR AGN identified by Symeonidis & Page (2021) are derived from the hard X-ray LF presented by Aird et al. (2015), the observed flattening at fainter luminosities is almost certainly due to X-ray emission not identifying the obscured faint AGN population. In contrast, SED fitting, as applied in our study, allows us to recover these faint AGN, providing a more complete picture of

Table 3. : CIGALE AGN LF  $\phi$  values.

$\log_{10}(L_{IR}/L_{\odot})$	$0.00 \leq z < 0.30$	$0.30 \leq z < 0.45$	$0.45 \leq z < 0.60$	$0.60 \leq z < 0.80$	$0.80 \leq z < 1.00$	$1.00 \leq z < 1.20$
8.00 – 8.25	$-2.57 \pm 0.12$	-	-	-	-	-
8.25 – 8.50	$-2.64 \pm 0.13$	-	-	-	-	-
8.50 – 8.75	$-2.84 \pm 0.16$	$-2.64 \pm 0.09$	-	-	-	-
8.75 – 9.00	$-2.74 \pm 0.14$	$-2.78 \pm 0.11$	$-2.58 \pm 0.07$	-	-	-
9.00 – 9.25	$-2.60 \pm 0.13$	$-2.90 \pm 0.13$	$-2.58 \pm 0.07$	$-2.48 \pm 0.04$	-	-
9.25 – 9.50	$-2.84 \pm 0.16$	$-2.98 \pm 0.14$	$-2.74 \pm 0.08$	$-2.69 \pm 0.05$	$-2.46 \pm 0.04$	-
9.50 – 9.75	-	$-2.90 \pm 0.13$	$-2.57 \pm 0.07$	$-2.76 \pm 0.06$	$-2.58 \pm 0.04$	$-2.67 \pm 0.04$
9.75 – 10.00	-	$-2.81 \pm 0.11$	$-2.79 \pm 0.09$	$-2.75 \pm 0.06$	$-2.91 \pm 0.06$	$-2.79 \pm 0.05$
10.00 – 10.25	-	$-2.78 \pm 0.11$	$-2.92 \pm 0.10$	$-2.80 \pm 0.06$	$-2.94 \pm 0.06$	$-2.98 \pm 0.06$
10.25 – 10.50	-	-	$-3.12 \pm 0.13$	$-3.28 \pm 0.11$	$-3.25 \pm 0.09$	$-3.12 \pm 0.07$
10.50 – 10.75	-	-	-	$-3.49 \pm 0.14$	-	$-3.54 \pm 0.12$
10.75 – 11.00	-	-	-	$-3.79 \pm 0.19$	-	$-3.73 \pm 0.14$
$\log_{10}(L_{IR}/L_{\odot})$	$1.20 \leq z < 1.70$	$1.70 \leq z < 2.00$	$2.00 \leq z < 2.50$	$2.50 \leq z < 3.00$	$3.00 \leq z < 4.20$	$4.20 \leq z < 6.00$
9.75 – 10.00	$-2.55 \pm 0.02$	-	-	-	-	-
10.00 – 10.25	$-2.68 \pm 0.02$	$-2.55 \pm 0.03$	-	-	-	-
10.25 – 10.50	$-2.91 \pm 0.03$	$-2.67 \pm 0.03$	$-2.63 \pm 0.02$	-	-	-
10.50 – 10.75	$-3.13 \pm 0.04$	$-2.85 \pm 0.04$	$-2.76 \pm 0.03$	$-2.76 \pm 0.03$	-	-
10.75 – 11.00	$-3.43 \pm 0.06$	$-3.02 \pm 0.05$	$-3.06 \pm 0.04$	$-2.84 \pm 0.03$	$-2.94 \pm 0.02$	-
11.00 – 11.25	$-4.02 \pm 0.12$	$-3.40 \pm 0.07$	$-3.13 \pm 0.04$	$-3.04 \pm 0.04$	$-3.08 \pm 0.02$	-
11.25 – 11.50	-	$-3.64 \pm 0.09$	$-3.39 \pm 0.05$	$-3.21 \pm 0.04$	$-3.35 \pm 0.03$	$-3.77 \pm 0.05$
11.50 – 11.75	-	$-4.03 \pm 0.14$	$-3.68 \pm 0.07$	$-3.55 \pm 0.06$	$-3.69 \pm 0.05$	$-4.14 \pm 0.07$
11.75 – 12.00	-	$-4.29 \pm 0.19$	$-4.32 \pm 0.15$	$-3.94 \pm 0.10$	$-4.03 \pm 0.07$	$-4.27 \pm 0.09$
12.00 – 12.25	-	-	-	$-4.52 \pm 0.19$	$-4.19 \pm 0.09$	$-4.78 \pm 0.15$

**Note:** Luminosity bin  $\phi$  values are centred.

the AGN population (Gruppioni et al. 2011; Brown et al. 2019; Thorne et al. 2022). Although not shown in Figure 3, the combined type-1 and type-2 AGN from Symeonidis & Page (2021) show elevated number densities, particularly in the  $1.2 \leq z < 2.5$  range, and align well with our CIGALE AGN results. This strong agreement underscores the robustness of our approach in isolating obscured faint AGN, especially at higher redshifts.

As the CIGALE AGN LF evolves with redshift, the faint end approaches the number density values of the CIGALE SF LF (discussed in the following subsection) at  $0 \leq z < 2.5$  and nearly surpasses them at  $z > 2.5$ . This trend aligns with the well-known peak of the cosmic SF of galaxies above  $z = 2$  (Madau & Dickinson 2014). Conversely, the AGN fraction increases with redshift and  $L_{IR}$  as noted by Symeonidis & Page (2021); Thorne et al. (2022) and references therein. Although our results do not yet show AGN number densities overtaking those of SF galaxies, future studies probing higher redshifts will likely reveal this transition, reflecting the dominance of AGN activity in the extremely early universe.

### 5.1.3. CIGALE SF

As seen in figure 3, the CIGALE SF LF is elevated above the ZFOURGE total and comparable literature LFs at brighter luminosities. We see excellent agreement between CIGALE SF and ZFOURGE LFs towards fainter luminosities. Several factors could contribute to this result. Work by Wu et al. (2011) has shown

that the UV and optical wavelengths follow a Schechter function closely. In contrast, the IR wavelengths have a shallower exponential which is inconsistent with a Schechter function (Symeonidis & Page 2019). Fu et al. (2010) proposed that this difference is due to the AGN contribution to the IR Galaxy LF. Wu et al. (2011) also concludes that the bright end slope is consistent with a Schechter function when AGN are removed. Given these findings, we argue that CIGALE accurately isolates the SF fraction and AGN contribution to galaxy emission. Although our results in figure 3 show fewer luminosity bins at the bright end, there are enough to constrain a well-defined Schechter functional fit.

As expected, the bright-end slope of a Schechter function is too steep to accurately describe the ZFOURGE total IR LF (Wu et al. 2011), in agreement with the literature (Rodighiero et al. 2010; Gruppioni et al. 2013; Symeonidis & Page 2019). Even after removing AGN-identified galaxies (552, Cowley et al. 2016), the ZFOURGE LFs do not show an improved Schechter function fit as predicted by Fu et al. (2010); Wu et al. (2011). The most likely reason is that Cowley et al. (2016) only identifies the most AGN-dominated sources, leaving fainter-luminosity AGN undetected. AGN activity and SFR are tightly coupled (Alexander & Hickox 2012 and references within), with both AGN activity and SF likely happening at the same time or in offset cycles (Cowley et al. 2018). At higher redshifts ( $z > 2$ ), it becomes increasingly essential to disentangle AGN and SF components of galaxy emission to model galaxy evolution accurately.



Table 4. : CIGALE SF LF  $\phi$  values.

$\log_{10}(L_{IR}/L_{\odot})$	$0.00 \leq z < 0.30$	$0.30 \leq z < 0.45$	$0.45 \leq z < 0.60$	$0.60 \leq z < 0.80$	$0.80 \leq z < 1.00$	$1.00 \leq z < 1.20$
8.50 – 8.75	$-1.74 \pm 0.05$	-	-	-	-	-
8.75 – 9.00	$-1.70 \pm 0.04$	-	-	-	-	-
9.00 – 9.25	$-1.83 \pm 0.05$	$-1.77 \pm 0.03$	-	-	-	-
9.25 – 9.50	$-1.83 \pm 0.05$	$-1.89 \pm 0.04$	$-1.90 \pm 0.03$	-	-	-
9.50 – 9.75	$-1.93 \pm 0.06$	$-2.00 \pm 0.04$	$-2.06 \pm 0.04$	$-1.90 \pm 0.02$	-	-
9.75 – 10.00	$-2.02 \pm 0.06$	$-2.03 \pm 0.05$	$-2.02 \pm 0.04$	$-1.91 \pm 0.02$	$-2.06 \pm 0.02$	-
10.00 – 10.25	$-2.14 \pm 0.07$	$-2.22 \pm 0.06$	$-2.17 \pm 0.04$	$-2.07 \pm 0.03$	$-2.08 \pm 0.02$	$-2.25 \pm 0.03$
10.25 – 10.50	$-2.16 \pm 0.08$	$-2.23 \pm 0.06$	$-2.25 \pm 0.05$	$-2.10 \pm 0.03$	$-2.20 \pm 0.03$	$-2.27 \pm 0.03$
10.50 – 10.75	$-2.32 \pm 0.09$	$-2.23 \pm 0.06$	$-2.39 \pm 0.05$	$-2.17 \pm 0.03$	$-2.30 \pm 0.03$	$-2.38 \pm 0.03$
10.75 – 11.00	$-2.32 \pm 0.09$	$-2.51 \pm 0.08$	$-2.39 \pm 0.05$	$-2.28 \pm 0.03$	$-2.37 \pm 0.03$	$-2.46 \pm 0.03$
11.00 – 11.25	$-2.64 \pm 0.13$	$-2.66 \pm 0.09$	$-2.57 \pm 0.07$	$-2.33 \pm 0.04$	$-2.43 \pm 0.04$	$-2.64 \pm 0.04$
11.25 – 11.50	-	$-3.08 \pm 0.15$	$-2.90 \pm 0.10$	$-2.40 \pm 0.04$	$-2.50 \pm 0.04$	$-2.70 \pm 0.04$
11.50 – 11.75	-	-	$-3.20 \pm 0.14$	$-2.72 \pm 0.06$	$-2.52 \pm 0.04$	$-2.68 \pm 0.04$
11.75 – 12.00	-	-	-	$-3.28 \pm 0.11$	$-2.82 \pm 0.06$	$-2.95 \pm 0.06$
12.00 – 12.25	-	-	-	$-3.79 \pm 0.19$	$-3.03 \pm 0.07$	$-3.43 \pm 0.10$
12.25 – 12.50	-	-	-	-	$-3.76 \pm 0.16$	$-3.78 \pm 0.15$
$\log_{10}(L_{IR}/L_{\odot})$	$1.20 \leq z < 1.70$	$1.70 \leq z < 2.00$	$2.00 \leq z < 2.50$	$2.50 \leq z < 3.00$	$3.00 \leq z < 4.20$	$4.20 \leq z < 6.00$
10.50 – 10.75	$-2.46 \pm 0.02$	$-2.64 \pm 0.03$	-	-	-	-
10.75 – 11.00	$-2.58 \pm 0.02$	$-2.59 \pm 0.03$	$-2.77 \pm 0.03$	-	-	-
11.00 – 11.25	$-2.61 \pm 0.02$	$-2.70 \pm 0.03$	$-2.79 \pm 0.03$	$-2.93 \pm 0.03$	-	-
11.25 – 11.50	$-2.67 \pm 0.02$	$-2.58 \pm 0.03$	$-2.76 \pm 0.03$	$-2.84 \pm 0.03$	-	-
11.50 – 11.75	$-2.65 \pm 0.02$	$-2.65 \pm 0.03$	$-2.76 \pm 0.03$	$-2.94 \pm 0.03$	$-3.17 \pm 0.03$	-
11.75 – 12.00	$-2.82 \pm 0.03$	$-2.73 \pm 0.03$	$-2.78 \pm 0.03$	$-3.01 \pm 0.03$	$-3.30 \pm 0.03$	$-3.74 \pm 0.05$
12.00 – 12.25	$-3.02 \pm 0.04$	$-2.87 \pm 0.04$	$-2.97 \pm 0.03$	$-3.17 \pm 0.04$	$-3.49 \pm 0.04$	$-4.03 \pm 0.06$
12.25 – 12.50	$-3.32 \pm 0.05$	$-3.11 \pm 0.05$	$-3.17 \pm 0.04$	$-3.34 \pm 0.05$	$-3.82 \pm 0.06$	$-4.24 \pm 0.08$
12.50 – 12.75	$-3.82 \pm 0.09$	$-3.39 \pm 0.07$	$-3.48 \pm 0.06$	$-3.54 \pm 0.06$	$-4.01 \pm 0.07$	$-4.91 \pm 0.18$
12.75 – 13.00	-	$-4.21 \pm 0.18$	$-3.92 \pm 0.10$	$-4.27 \pm 0.14$	$-4.43 \pm 0.12$	$-4.91 \pm 0.18$

**Note:** Luminosity bin  $\phi$  values are centred.

#### 5.1.4. Combined Evolution

In figure 4, we show the combined evolution of the ZFOURGE bolometric IR (8-1000 $\mu$ m) LF. The LF is filled between the  $1\sigma$  uncertainty bounds, calculated using equation 3. With this figure, it is easier to see the evolution of the LF across luminosity and redshift. A clear declining density trend is seen with increasing luminosity and redshift.

This result is significant because it highlights how the relative contributions of SF and AGN activity evolve. Both SF and AGN number densities increase with luminosity as the universe ages towards the present day. This suggests a tentative downsizing effect, which we explore further in section 5.4. The decline in the LF with increasing luminosity and redshift suggests that the early universe contained fewer luminous galaxies, implying lower overall SF and AGN activity. As we move towards the present day, the rising number density of bright galaxies in the LF (until the lowest redshift bins) reflects the growth and evolution of galaxies and their central SMBHs, with an increase in both SF and AGN contributions.

#### 5.2. Parameter Evolution

In this section, we discuss the parameter evolution of the Saunders and Schechter luminosity function fits in figure 3. The evolution of  $\phi^*$  and  $L^*$  across redshift is presented in figure 5 with values and  $1\sigma$  errors in tables 5, 6, and 7. The best fitting parameter values were calculated using `scipy.optimize.curve_fit` (Virtanen et al. 2020) and  $1\sigma$  parameter uncertainties are calculated using `np.sqrt(np.diag(pcov))` (Harris et al. 2020) which relates the covariance of the best-fit parameters. As discussed in section 5.1, our final redshift bin likely suffers from incompleteness. However, ZFOURGE's ability to probe fainter luminosities becomes advantageous at higher redshifts, providing more reliable constraints on the LF parameters. In our lowest redshift bins, where ZFOURGE is less effective, more pronounced  $1\sigma$  errors are recorded.

To better constrain the faint end slope of the ZFOURGE total LF, we fix  $\alpha = 1.3$  across all redshift bins. This result differs from the literature where Rodighiero et al. (2010); Gruppioni et al. (2013) fix  $\alpha = 1.2$  whereas Fu et al. (2010) leaves  $\alpha$  as a free fitting parameter found to be  $\alpha = 1.46$  (relative to our Saunders fitting function). As we lack luminosity bins along the bright end

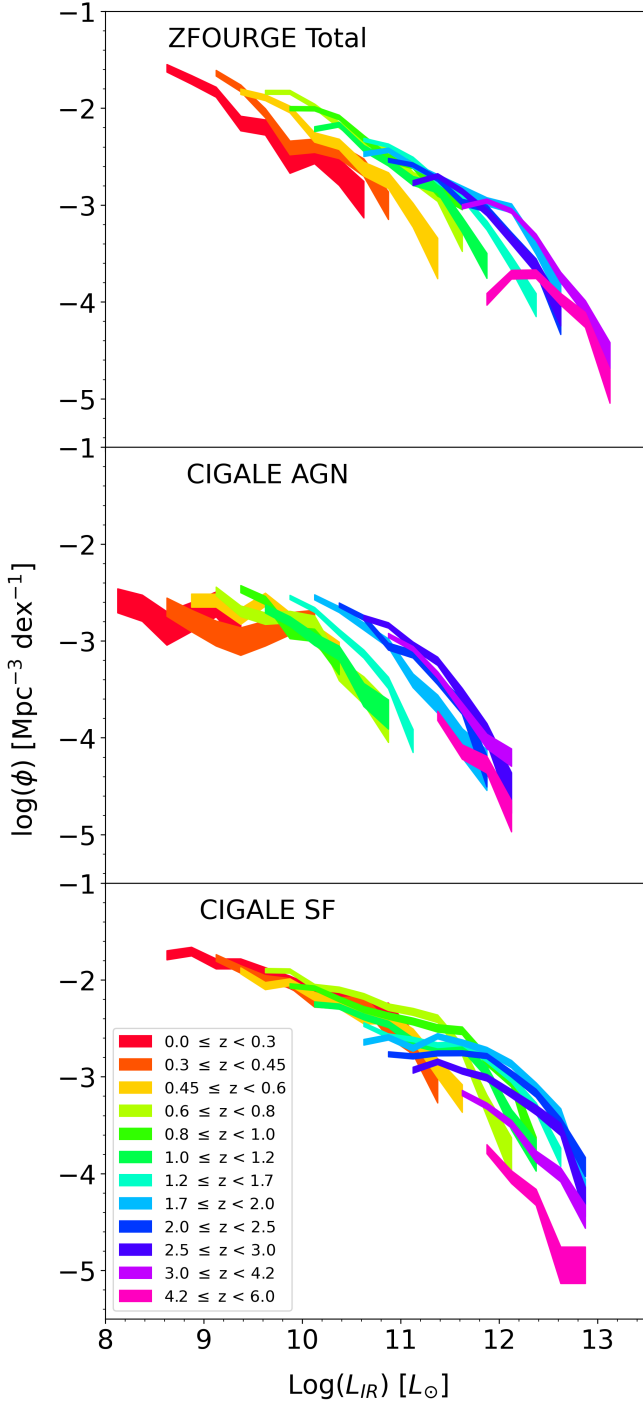


**Figure 4:** Combined evolution of the ZFOURGE total (top), CIGALE AGN (middle), and CIGALE SF (bottom) luminosity functions shown in figure 3. The redshift evolution of each binned LF is easier to visualise. Data points are shaded between the  $1\sigma$  uncertainties and coloured by redshift bin.

of the LF, we fix the bright end  $\sigma$  to values that fit best to the available literature. The CIGALE SF LF fits with a Schechter function and a faint end slope of  $\alpha = 1.2$ , reflecting its shallower rise compared to the ZFOURGE total LF. Similarly, we use a Saunders function to fit the CIGALE AGN LF using  $\alpha = 1.2$ . The faint end slopes of CIGALE LFs agree with the literature. Due to the

absence of bright-end AGN luminosity bins, we incorporate data from Thorne *et al.* (2022) to help constrain the fitting process.

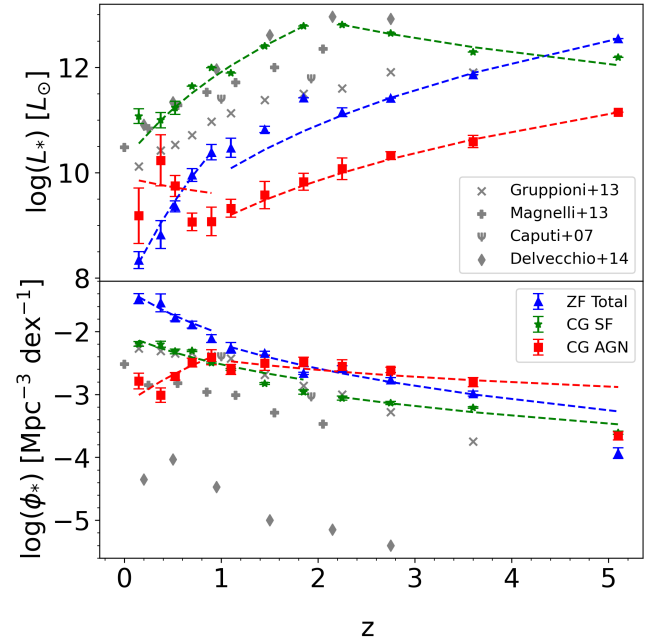


**Figure 5:** Best fitting parameters and  $1\sigma$  uncertainties to our luminosity functions. Top:  $L^*$  evolution. Bottom:  $\phi^*$  evolution. Blue triangles represent the ZFOURGE total. Red squares represent the CIGALE AGN and green crosses the CIGALE SF population. Dashed lines represent the  $\propto (1+z)^k$  evolution. We compare our results to the relevant literature, which is coloured grey. Gruppioni *et al.* (2013) crosses, Magnelli *et al.* (2013) pluses, and Caputi *et al.* (2007) uppercase  $\Psi$ 's.

**Table 5. :** Best-fit parameters ( $\log(L^*)$ ,  $\log(\phi^*)$ ), along with fixed parameters ( $\alpha$ ,  $\sigma$ ), for the ZFOURGE total Saunders luminosity function across different redshift bins.

$z$	$\log(L^*)$	$\log(\phi^*)$	$\alpha$	$\sigma$
$0.00 \leq z < 0.30$	$8.34 \pm 0.16$	$-1.48 \pm 0.08$	1.3	1.1
$0.30 \leq z < 0.45$	$8.82 \pm 0.26$	$-1.54 \pm 0.14$	1.3	1.0
$0.45 \leq z < 0.60$	$9.36 \pm 0.10$	$-1.78 \pm 0.05$	1.3	0.9
$0.60 \leq z < 0.80$	$9.96 \pm 0.12$	$-1.89 \pm 0.05$	1.3	0.8
$0.80 \leq z < 1.00$	$10.39 \pm 0.14$	$-2.11 \pm 0.06$	1.3	0.7
$1.00 \leq z < 1.20$	$10.47 \pm 0.18$	$-2.26 \pm 0.09$	1.3	0.7
$1.20 \leq z < 1.70$	$10.82 \pm 0.06$	$-2.35 \pm 0.03$	1.3	0.7
$1.70 \leq z < 2.00$	$11.42 \pm 0.00$	$-2.67 \pm 0.02$	1.3	0.7
$2.00 \leq z < 2.50$	$11.14 \pm 0.08$	$-2.58 \pm 0.04$	1.3	0.7
$2.50 \leq z < 3.00$	$11.42 \pm 0.00$	$-2.77 \pm 0.03$	1.3	0.7
$3.00 \leq z < 4.20$	$11.86 \pm 0.00$	$-2.99 \pm 0.04$	1.3	0.7
$4.20 \leq z < 6.00$	$12.54 \pm 0.00$	$-3.93 \pm 0.08$	1.3	0.7

Our ZFOURGE free parameters  $L^*$  and  $\phi^*$  exhibit evolutionary trends that differ from those reported in the literature. However,

Table 6. : Best-fit parameters ( $\log(L^*)$ ,  $\log(\phi^*)$ ), along with fixed parameters ( $\alpha$ ,  $\sigma$ ), for the CIGALE AGN Saunders luminosity function across different redshift bins.

$z$	$\log(L^*)$	$\log(\phi^*)$	$\alpha$	$\sigma$
$0.00 \leq z < 0.30$	$9.19 \pm 0.53$	$-2.79 \pm 0.13$	1.2	1.0
$0.30 \leq z < 0.45$	$9.99 \pm 0.59$	$-2.96 \pm 0.14$	1.2	1.0
$0.45 \leq z < 0.60$	$9.42 \pm 0.26$	$-2.65 \pm 0.08$	1.2	1.0
$0.60 \leq z < 0.80$	$9.07 \pm 0.17$	$-2.49 \pm 0.07$	1.2	1.0
$0.80 \leq z < 1.00$	$9.07 \pm 0.27$	$-2.41 \pm 0.12$	1.2	1.0
$1.00 \leq z < 1.20$	$9.32 \pm 0.17$	$-2.60 \pm 0.08$	1.2	1.0
$1.20 \leq z < 1.70$	$9.57 \pm 0.26$	$-2.50 \pm 0.12$	1.2	1.0
$1.70 \leq z < 2.00$	$9.82 \pm 0.16$	$-2.49 \pm 0.07$	1.2	1.0
$2.00 \leq z < 2.50$	$10.07 \pm 0.20$	$-2.55 \pm 0.10$	1.2	0.9
$2.50 \leq z < 3.00$	$10.32 \pm 0.07$	$-2.61 \pm 0.04$	1.2	0.8
$3.00 \leq z < 4.20$	$10.59 \pm 0.12$	$-2.81 \pm 0.07$	1.2	0.7
$4.20 \leq z < 6.00$	$11.15 \pm 0.00$	$-3.66 \pm 0.07$	1.2	0.6

Table 7. : Best-fit parameters ( $\log(L^*)$ ,  $\log(\phi^*)$ ), along with fixed parameter ( $\alpha$ ), for the CIGALE SF Schechter luminosity function across different redshift bins.

$z$	$\log(L^*)$	$\log(\phi^*)$	$\alpha$
$0.00 \leq z < 0.30$	$11.07 \pm 0.14$	$-2.20 \pm 0.04$	1.2
$0.30 \leq z < 0.45$	$11.00 \pm 0.15$	$-2.20 \pm 0.05$	1.2
$0.45 \leq z < 0.60$	$11.23 \pm 0.12$	$-2.32 \pm 0.04$	1.2
$0.60 \leq z < 0.80$	$11.64 \pm 0.00$	$-2.31 \pm 0.01$	1.2
$0.80 \leq z < 1.00$	$11.99 \pm 0.00$	$-2.50 \pm 0.01$	1.2
$1.00 \leq z < 1.20$	$11.89 \pm 0.00$	$-2.60 \pm 0.02$	1.2
$1.20 \leq z < 1.70$	$12.40 \pm 0.00$	$-2.83 \pm 0.02$	1.2
$1.70 \leq z < 2.00$	$12.78 \pm 0.00$	$-2.96 \pm 0.03$	1.2
$2.00 \leq z < 2.50$	$12.81 \pm 0.00$	$-3.06 \pm 0.03$	1.2
$2.50 \leq z < 3.00$	$12.65 \pm 0.00$	$-3.13 \pm 0.02$	1.2
$3.00 \leq z < 4.20$	$12.29 \pm 0.00$	$-3.21 \pm 0.01$	1.2
$4.20 \leq z < 6.00$	$12.19 \pm 0.00$	$-3.61 \pm 0.02$	1.2

our fitting process is robust, and the evolution of the free parameters does not change significantly when the fixed parameters are altered. A known challenge in this analysis is the degeneracy between  $L^*$  and  $\phi^*$ . A decrease in  $L^*$  can be somewhat compensated for by increasing  $\phi^*$  and vice-versa. Thus, the absolute values of the parameters themselves can be overlooked in favour of the overall trend in the dataset.

As shown below, we find rapid evolution of ZFOURGE  $L^*$  up to  $z \approx 1$ , after which  $L^*$  evolution slows. ZFOURGE  $\phi^*$  does not show as rapid evolution as  $L^*$  in all redshift bins:

$$L^* = \begin{cases} 10^{7.70 \pm 0.14} \times (1+z)^{9.64 \pm 0.51} & \text{for } z < 1, \\ 10^{8.37 \pm 0.28} \times (1+z)^{5.31 \pm 0.36} & \text{for } z > 1. \end{cases}$$

$$\phi^* = \begin{cases} 10^{-1.30 \pm 0.07} \times (1+z)^{-2.44 \pm 0.52} & \text{for } z < 1, \\ 10^{-1.54 \pm 0.12} \times (1+z)^{-2.21 \pm 0.31} & \text{for } z > 1. \end{cases}$$

Compared to the literature, both Gruppioni et al. (2013) and Magnelli et al. (2013) find much shallower  $L^*$  evolution from  $0 < z < 1$ . ZFOURGE evolves 2-3x faster at  $0 < z < 1$ , but only 1.25x faster at  $z > 1$ . This could be explained by ZFOURGE probing fainter luminosities. However, it is important to note that ZFOURGE was optimised for studying galaxies at  $z > 1$ , where its deep near-infrared coverage is particularly effective. Consequently, results at  $z < 1$  should be interpreted cautiously, as the survey's design is less tailored to these lower redshifts.

The CIGALE SF  $L^*$  shows slower evolution compared to the ZFOURGE total from  $0 < z < 1$  but similar evolution from  $1 < z < 2$ . In contrast to ZFOURGE results, the CIGALE SF  $L^*$  declines from  $z > 2$  onwards.

$$L^* = \begin{cases} 10^{10.21 \pm 0.16} \times (1+z)^{5.65 \pm 0.36} & \text{for } z < 2, \\ 10^{14.24 \pm 0.25} \times (1+z)^{-2.80 \pm 0.45} & \text{for } z > 2. \end{cases}$$

This reversal is not seen in the evolution of  $\phi^*$ , which has a similar slope across all redshifts and is close to the results published by Magnelli et al. (2013).

$$\phi^* = \begin{cases} 10^{-2.05 \pm 0.05} \times (1+z)^{-1.58 \pm 0.28} & \text{for } z < 2, \\ 10^{-2.24 \pm 0.12} \times (1+z)^{-1.58 \pm 0.40} & \text{for } z > 2. \end{cases}$$

The reversal in the evolution of  $L^*$  above  $z > 2$  indicates that SF grew from at least  $z = 5$  to  $z = 2$  and has been declining ever since. It is well known (Gruppioni et al. 2013; Madau & Dickinson 2014 and references within) that the IR luminosity density has been declining since  $z \approx 2$  and we explore this possibility more in section 5.3. Gruppioni et al. (2013) and Magnelli et al. (2013) find similar results in  $L^*$  from  $0 < z < 1$  and similar  $\phi^*$  evolution from  $0 < z < 2$ .

The CIGALE AGN  $L^*$  and  $\phi^*$  evolve in the opposite direction from the literature and from our ZFOURGE and CIGALE SF parameters at  $z < 1$ :

$$L^* = \begin{cases} 10^{9.92 \pm 0.61} \times (1+z)^{-1.09 \pm 3.62} & \text{for } z < 1, \\ 10^{7.85 \pm 0.11} \times (1+z)^{4.20 \pm 0.15} & \text{for } z > 1. \end{cases}$$

$$\phi^* = \begin{cases} 10^{-3.18 \pm 0.19} \times (1+z)^{2.77 \pm 0.80} & \text{for } z < 1, \\ 10^{-2.19 \pm 0.20} \times (1+z)^{-0.88 \pm 0.42} & \text{for } z > 1. \end{cases}$$

At  $z > 1$ , the evolution follows the normal trend. This anomalous behavior at  $z < 1$  could be attributed to the degeneracy between  $L^*$  and  $\phi^*$ , as previously mentioned. However, the magnitude of this degeneration has not been observed so prominently in the literature, suggesting two possibilities: CIGALE reveals a significant evolutionary epoch for AGN at  $z \approx 1$ , or there is a bias in our fitting process. The fact that our fitting process produces similar results for the ZFOURGE total as seen in the literature and recovers the peak and turnover in the CIGALE SF gives good evidence to the idea that  $z \approx 1$  is a significant epoch for AGN evolution. Hopkins et al. (2007) and Delvecchio et al. (2014) show a similar reversal and subsequent decline in  $\phi^*$  evolution below  $z = 1$ . However, both do not find a corresponding reversal and uptick in  $L^*$  evolution at  $z = 1$ . Katsianis et al. (2017) shows that

high SFG rapidly decline below  $z \approx 1$  because of AGN feedback. We are therefore confident in our CIGALE AGN results.

Our results are complex, but showcase the importance of decomposing the SED of galaxies to separate the SF and AGN components. These trends indicate significant shifts in AGN and SF activity over cosmic time that were not detected in the combined ZFOURGE total evolution.

### 5.3. Bolometric IR Luminosity Density

In this section, we calculate and analyse the bolometric IR (8–1000 $\mu\text{m}$ ) luminosity density (LD) and star formation rate density ( $\rho_{\text{SFRD}}$ ). Figure 6 shows the IR LD ( $\rho_{\text{IR}}$ ) of our ZFOURGE and CIGALE results with values in table 8. At each redshift bin,  $\rho_{\text{IR}}$  is calculated by integrating under the best fitting luminosity function with equation 6. Where  $\phi(L)$  is the best fitting luminosity function (in our case, the Schechter or Saunders function: equations 4 and 5 respectively). Schechter is used for the CIGALE SF, whereas Saunders is used for ZFOURGE total and CIGALE AGN. We utilise `scipy.integrate.quad` (Virtanen *et al.* 2020) to perform the integration from 0 to  $\infty L_{\odot}$  by cumulatively summing the integrand at incremental bounds (e.g. from  $10^{10}$  to  $10^{12} L_{\odot}$ ,  $10^{12}$  to  $10^{14} L_{\odot}$ , etc) because the quadrature algorithm isn't well suited for small areas over very large bounds. In practice, additional calculations of  $\rho_{\text{IR}}$  above  $10^{20} L_{\odot}$  are negligible. To generate  $1\sigma$   $\rho_{\text{IR}}$  uncertainties, we re-perform the integration using the  $1\sigma$  LF fit errors.

$$\rho_{\text{IR}} = \frac{1}{\ln(10)} \int_0^{\infty} \phi(L) dL \quad (6)$$

Table 8. : Luminosity density as a function of redshift. Units are in  $\log(\rho_{\text{IR}}) [L_{\odot} \text{Mpc}^{-3}]$ . Errors are absolute.  $\rho_{\text{IR}}$  values are centered on the redshift bin.

$z$	ZFOURGE Total	CIGALE SF	CIGALE AGN
$0.00 \leq z < 0.30$	$7.98^{0.27}_{0.21}$	$8.58^{0.19}_{0.16}$	$7.53^{0.80}_{0.37}$
$0.30 \leq z < 0.45$	$8.24^{0.49}_{0.32}$	$8.50^{0.21}_{0.18}$	$7.81^{0.73}_{0.40}$
$0.45 \leq z < 0.60$	$8.38^{0.16}_{0.14}$	$8.62^{0.17}_{0.15}$	$7.62^{0.29}_{0.23}$
$0.60 \leq z < 0.80$	$8.72^{0.19}_{0.16}$	$9.04 \pm 0.01$	$7.70^{0.26}_{0.21}$
$0.80 \leq z < 1.00$	$8.79^{0.22}_{0.18}$	$9.20 \pm 0.01$	$7.80^{0.46}_{0.31}$
$1.00 \leq z < 1.20$	$8.72^{0.30}_{0.23}$	$8.99 \pm 0.02$	$7.85^{0.28}_{0.22}$
$1.20 \leq z < 1.70$	$8.98^{0.09}_{0.08}$	$9.28 \pm 0.02$	$8.20^{0.45}_{0.31}$
$1.70 \leq z < 2.00$	$9.27 \pm 0.02$	$9.52 \pm 0.03$	$8.47^{0.26}_{0.21}$
$2.00 \leq z < 2.50$	$9.07^{0.13}_{0.12}$	$9.45 \pm 0.03$	$8.46^{0.36}_{0.26}$
$2.50 \leq z < 3.00$	$9.16 \pm 0.03$	$9.22 \pm 0.02$	$8.47^{0.12}_{0.11}$
$3.00 \leq z < 4.20$	$9.38 \pm 0.04$	$8.78 \pm 0.01$	$8.37^{0.21}_{0.17}$
$4.20 \leq z < 6.00$	$9.12 \pm 0.08$	$8.28 \pm 0.02$	$7.91 \pm 0.07$

The secondary right-hand-side axis of figure 6 displays the conversion to SFRD provided by Kennicutt (1998) calculated with  $\rho_{\text{SFRD}} = \rho_{\text{IR}} \times 1.7 \times 10^{-10} L_{\odot}$ . We remind the reader that the IR AGN densities do not have an associated SFR. The top x-axis shows the lookback time in billions of years, placing the evolution of the universe in the context of time to showcase the important evolutionary epochs.

Our ZFOURGE results in figure 6 show rapid evolution from  $0 < z < 2$ . From  $z > 2$  onwards, there is essentially no evolution. As discussed in section 5.2, our highest redshift bin was thought to suffer from incompleteness, but our  $\rho_{\text{IR}}$  results do not obviously show it. We see excellent agreement with the literature from  $0 < z < 2$  but deviate significantly from  $z > 2$  onwards. Importantly, we do not find a turnover in the IR LD at  $z \approx 2$ . This is a different result than is often published in the literature (Grupponi *et al.* 2013; Magnelli *et al.* 2013; Madau & Dickinson 2014; Lutz 2014 and references within). However, this is not a new result as is seen in Rodighiero *et al.* (2010), but they do not probe to a sufficiently high enough redshift to capture the decline above  $z > 2$ .

The CIGALE decomposed SF IR LD is seen to increase from  $0 < z < 2$  and decline from  $z > 2$  onwards. This agrees well with the literature, especially Madau & Dickinson (2014). The ability of CIGALE to recover the turnover in the SF IR LD, where ZFOURGE does not, suggests that CIGALE is effectively isolating the SF component and lends confidence to the accuracy of our results. The CIGALE SF LD is slightly elevated over ZFOURGE at most redshift bins. We believe this is not an error on CIGALE's part or the ZFOURGE data it is based on, but a representation of the true pure SF IR LD because AGN contaminants have been effectively eliminated. As mentioned previously in section 5.1, both Fu *et al.* (2010) and Wu *et al.* (2011) argue that when AGN are removed, the luminosity function is better fit with a Schechter function. This agrees with our results and explains why our CIGALE SF LFs (figure 3) are elevated. Integrating under the CIGALE SF Schechter functions, we see an elevation in  $\rho_{\text{IR}}$ .

The CIGALE AGN LD follows a similar evolution to the literature, though it is elevated, likely due to CIGALE's ability to detect fainter AGN. The trend seen in the CIGALE SF LD increasing from  $0 < z < 2$  and declining from  $z > 2$  is still present in the AGN LD. This is not the first time a turnover in the AGN  $\rho_{\text{IR}}$  has been seen. Symeonidis & Page (2021) presents their IR AGN densities up to  $z \approx 2.5$ . These results are at most  $\approx 1$  order of magnitude lower than ours. We attribute this to their use of Aird *et al.* (2015) X-ray sources, which are converted to optical luminosity and then to IR luminosity. Their X-ray-selected galaxies likely miss the highly obscured and faint-luminosity counterpart that this work recovers. As Symeonidis & Page (2021) only extends as far as  $z \approx 2.5$ , the AGN  $\rho_{\text{IR}}$  turnover is not well defined. AGN by Delvecchio *et al.* (2014) agrees well with our results. We recalculated the AGN  $\rho_{\text{IR}}$  for the Delvecchio *et al.* (2014) dataset because they did not provide  $\rho_{\text{IR}}$  values in their work, instead focusing on the black hole accretion rate density ( $\Psi_{\text{bhar}}$ ). Using the function parameters they reported, we use the same integration method described previously to calculate  $\rho_{\text{IR}}$ .

Both Symeonidis & Page (2021) and Delvecchio *et al.* (2014) show AGN LD peaks at  $z \approx 2$  whereas our CIGALE AGN LD peaks sometime between  $z \approx 2 - 3$ . As was mentioned in section 5.2, there appeared to be a significant evolutionary epoch for AGN occurring at  $z \approx 1$ . Despite the parameter evolution (Figure 5) seemingly hinting at a significant cosmic epoch for AGN evolution, we do not obviously see this reflected in our AGN LD results. From  $0 < z < 2$ , AGN density is seen to decline, albeit slowly and with some scatter. Our two lowest redshift bins have high uncertainties, so there remains the possibility that somewhere between  $0 < z < 1$  is a significant time for AGN evolution. Therefore, relying solely on the LD evolution of AGN and SF galaxies to assess their overall evolution may oversimplify their complex evolution. The functional fits smoothed out slight variations in the LF, potentially masking essential details.

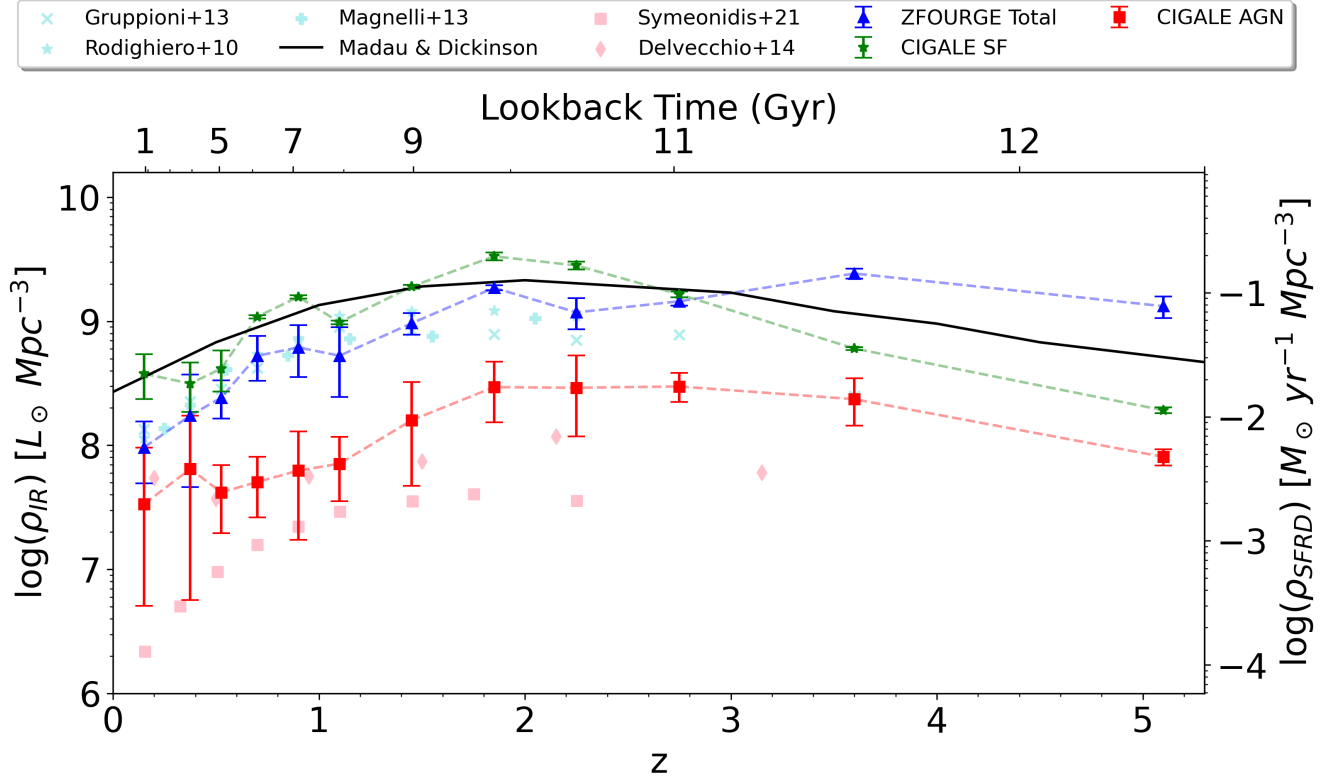


**Figure 6:** Evolution of the IR luminosity density (LD) calculated by integrating under the best fitting LFs.  $1\sigma$  uncertainties are calculated by re-performing the integration with errors from the LF fitting process. Saunders is fit for the ZFOURGE total and CIALE AGN, whereas Schechter is fit for the CIGALE SF. Blue triangles represent ZFOURGE total; green stars CIGALE SF; and red squares CIGALE AGN. The right side y-axis is obtained from Kennicutt (1998) with  $\rho_{SFRD} = \rho_{IR} \times 1.7 \times 10^{-10} L_{\odot}$ . The top axis shows the lookback time in billions of years. We compare our results with relevant literature. Gruppioni et al. (2013); Rodighiero et al. (2010); Magnelli et al. (2013) as light blue compare the SF LD. Symeonidis & Page (2021) and Delvecchio et al. (2014) as light red compare the AGN LD. The solid black line is the Madau & Dickinson (2014) LD.

#### 5.4. Space Density Evolution

In this section, we inspect the evolution of different luminosity classes by visualising the number density of each luminosity bin across redshift (figure 7). By incorporating the class density evolution into our analysis, a better picture of the evolution of galaxies and the co-evolution of AGN can be ascertained. When possible, the  $\phi$  values are taken from the existing luminosity bins<sup>b</sup>. Otherwise,  $\phi$  values are calculated from the best-fitting LF. The class density evolution (figure 7) can be thought of as the transposition of the LF (figures 3 and 4). The LF and class density are complementary because they allow us to view the number density as an evolution with luminosity and redshift, respectively.

In figure 7, we present IR luminosity classes as low as  $L_{IR} = 10^{8.5} L_{\odot}$ . We find that the space density of ZFOURGE LIRGs and ULIRGs have been consistently declining since at least  $z = 2$ , and likely even earlier for ULIRGs. Galaxies fainter than LIRGs (FIRGs,  $L_{IR} < 10^{11} L_{\odot}$ ) evolve differently, beginning to decline at a lower redshift than their brighter luminosity counterparts. The redshift at which galaxies begin declining in number density is related to their luminosity. ZFOURGE galaxies fainter than  $L_{IR} < 10^9 L_{\odot}$  appear to be increasing in number density across

all of cosmic time and have yet to begin declining. We find similar agreement in the literature with Rodighiero et al. (2010) and Gruppioni et al. (2013) with our results mostly in agreement. We attribute the differences to slight variations in the classes and methods within. FIRGs dominate the ZFOURGE LD from  $0 < z < 0.8$ , declining from 74% to 51%. From  $0.8 < z < 1.7$ , LIRGs dominate LD, remaining steady with 45% to 47% contribution. At  $z > 1.7$ , ULIRGs dominate LD, increasing rapidly from 59% to 92%. In the highest redshift bin, FIRG contribution drops to less than 2%.

CIGALE SF galaxies evolve differently from ZFOURGE, although similar contributions to the LD are seen. FIRGs dominate LD density from  $0 < z < 0.8$ , declining from 80% to 47%. LIRGs only dominate LD from  $0.8 < z < 1.2$  with 50% contribution. ULIRGs dominate LD from  $z > 1.2$  onwards, generally increasing over time with some scatter. Figure 7 shows that SF LIRGs evolve similarly to FIRGs at  $z > 2$ . Although, the estimated  $\phi$  values show increasing number density with decreasing luminosity for all FIRGs. One real  $\phi$  value exists in the brightest luminosity class ( $10^{13} < L_{IR} < 10^{13.5} L_{\odot}$ ) in our highest redshift bin which is only slightly lower in number density than the previous luminosity class. This is possibly evidence of the Saunders function being a decent fit for the SF LF. A possible evolution scenario is theorised for SFG: all FIRGs evolve similarly from

<sup>b</sup>  $\phi$  values were recomputed with luminosity bins  $0.5 \log_{10}(L_{\odot})$  wide

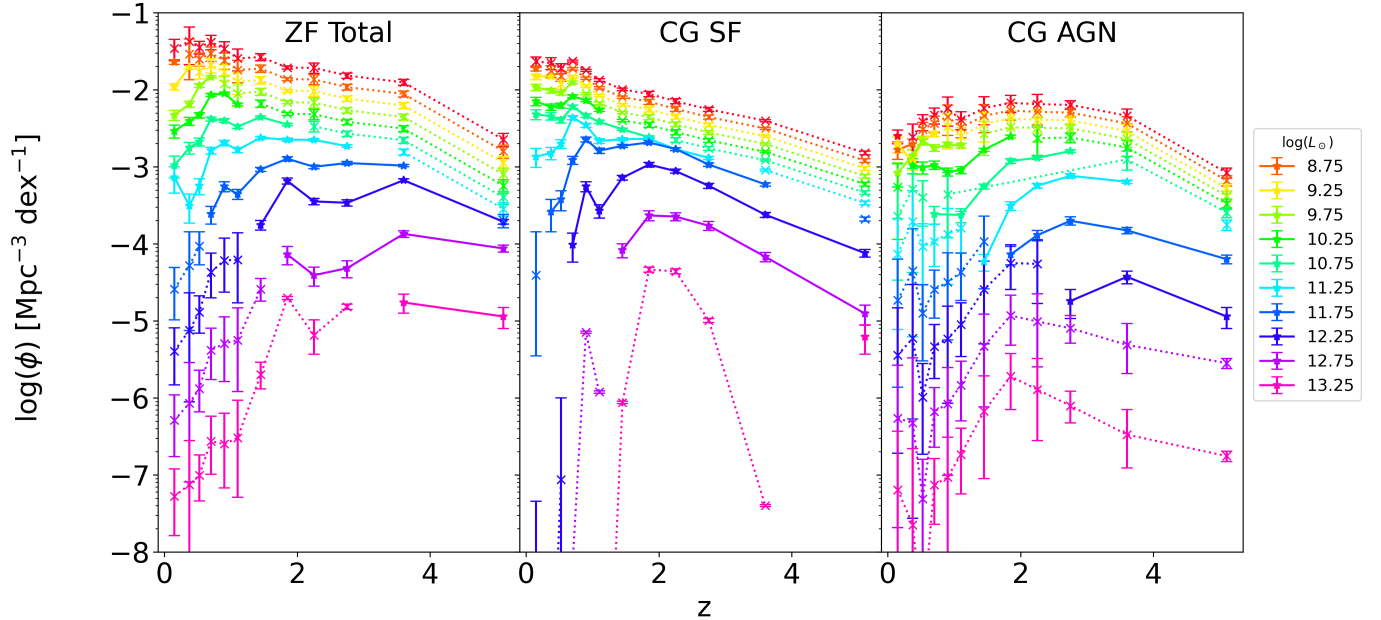


**Figure 7:** Luminosity class evolution as a function of redshift.  $\phi$  values connected by straight lines correspond to real calculated values.  $\phi$  values connected by dotted lines are estimated from the best fitting function (Schechter for CIGALE SF, Saunders for ZFOURGE Total and CIGALE AGN). Error bars represent the  $1\sigma$  uncertainty calculated with equation 3 for real values or derived from the function fitting process for estimated values. Real luminosity classes are  $0.5 \log(L_{\odot})$  in width and centred in the middle (e.g. 8.5 — 9.0 is centred on 8.75). Estimated classes are calculated at the centre of the luminosity bin (e.g. 8.75).

high redshift to  $z \approx 2$ , increasing in number density from high redshift. At and below  $z \approx 2$ , the brightest FIRG number densities begin to peak and decline earlier than fainter FIRG counterparts, which have yet to start declining. LIRGs decline faster and earlier than FIRGs, and ULIRGs decline faster and sooner than LIRGs. This reflects a *downsizing* scenario in which brighter galaxies peak in number density at higher redshift (Merloni & Heinz 2008; Wylezalek *et al.* 2014; Fiore *et al.* 2017).

CIGALE AGN again evolve differently. Faint IR AGN dominate LD from  $0 \leq z < 1.2$  and luminous IR AGN dominate LD from  $z > 1.2$  onwards. Ultra-luminous IR AGN never dominates LD. Unlike SF galaxies, the difference between FIRGs and LIRGs is stark. There is a clear, systematic shift of the peak number density with luminosity class. The *downsizing* seen in SF galaxies is more pronounced in AGN. As AGN luminosity increases, the number density of AGN peaks at higher redshifts and declines earlier than their fainter luminosity counterparts. When comparing the *downsizing* effect between SFGs and AGN, it is unmistakable that galaxies with a luminous AGN decline faster and earlier than equally bright SFG counterparts.

## 6. Conclusion

We utilised ZFOURGE data as inputs for CIGALE to separate the SF and AGN components of the infrared spectral energy distribution to create and analyse their respective luminosity functions. Our results are summarised as follows:

- (i) We first generate LFs of ZFOURGE galaxies from a subsample of 16,154 galaxies that accounted for incompleteness and bias across various redshift bins ranging from  $0 < z < 6$ .
- (ii) After CIGALE decomposition, we find 12,390 sources (16.8% of the sample) with a significant AGN fraction

( $\mathcal{F}_{AGN} > 0.1$ ). This reduces to 8,800 sources (11.9%) after incompleteness and bias are accounted for. In context with AGN dominant sources removed in ZFOURGE by Cowley *et al.* (2016), simple MIR colour-colour selection diagnostics are insufficient to identify low luminosity AGN, which we show significantly influences galaxy samples.

- (iii) We find that CIGALE SF LFs are a better fit with a Schechter function, as predicted by Wu *et al.* (2011); Fu *et al.* (2010). Although there is minor evidence that Saunders could fit better, brighter SF galaxies at higher redshifts are required to confirm.
- (iv) A peak and turnover in the evolution of CIGALE SF  $L^*$  is found at  $z \approx 2$  coinciding with the peak of cosmic star formation. Similarly, SF LD is also seen to peak and decline above  $z \approx 2$ . This agrees with established literature and provides good evidence supporting our CIGALE results. Importantly, no turnover in ZFOURGE LD was found, highlighting the importance of SED decomposition.
- (v) A turn over in  $L^*$  (minimum) and  $\phi^*$  (maximum) is seen for CIGALE AGN at  $z \approx 1$ . However, the AGN LD is not found to change significantly as the simultaneous change in parameters is thought to mostly balance out the difference. Delvecchio *et al.* (2014) finds a similar trend at the same time for their AGN  $L^*$ . Katsianis *et al.* (2017) also shows AGN feedback significantly affects SF at  $z < 1$ . We have found reliable evidence that  $z \approx 1$  is a significant evolutionary epoch for AGN evolution.
- (vi) In context, the time between the peak of SF  $L^*$  ( $z \approx 2$ ) and the minimum of AGN  $L^*$  ( $z \approx 1$ ) represents  $\approx 2.5 - 3$  Gyrs of evolution. SF  $\phi^*$  has increased at the same rate across all cosmic time and has yet to peak conclusively, but  $z \approx 0.5$  is a possible candidate. On the other-hand, AGN  $\phi^*$  reaches

- a peak at  $z \approx 1$  and a local minimum at  $z \approx 0.5$ , also representing  $\approx 2.5 - 3$  Gyrs of evolution. This is evidence of an AGN-SF feedback mechanism, which also appears cyclical.
- (vii) The space density evolution of luminosity classes for SFG and AGN are very different. LIRGs and ULIRGs increase in number density and peak at  $z \approx 2$  before rapidly declining to the present day. SF FIRGs evolve similarly across fainter luminosities and peak at a lower redshift. The faintest FIRGs have yet to peak in number density. AGN number densities peak much earlier in the universe than SF counterparts. Luminous and ultraluminous AGN have declined since at least  $z \approx 3$ . There is a strong correlation between peak AGN density and luminosity. Fainter AGN peak much later in the universe and have declined since  $z \approx 2$ . This shows a clear *downsizing* effect.
- (viii) From high redshift until  $z \approx 2$ , SFGs form with increasing brightness and consume a significant fraction of the available gas supply. SFGs form at a roughly constant rate across cosmic time, just not as big and bright at  $z < 2$  as the gas supply becomes increasingly exhausted. This is reflected in our class evolution results and is the likely reason behind the *downsizing* effect.
- (ix) Conversely, AGN are brightest at the beginning of time and decline in brightness at a constant rate until  $z \approx 1$ , where AGN power increases until  $z \approx 0.5$  before declining again. This reflects a period where the available gas supply shifted to fueling AGN growth.

These results indicate a feedback scenario with  $\approx 2.5 - 3$  Gyrs of evolution between each cycle. The available gas supply favoured SFG from high redshift until  $z \approx 2$  when the supply becomes increasingly exhausted. From  $1 < z < 2$ , the remaining gas was split into forming fainter stars and falling inwards towards the central SMBH. From  $0.5 < z < 1$ , AGN power significantly increased and consumed large fractions of the remaining gas to fuel itself, leaving even less for SF.

## Acknowledgements

This research was supported by an Australian Government Research Training Program (RTP) Scholarship.

## Data Availability

Python notebooks and scripts that analysed the data are available on GitHub at <https://github.com/daniel-lyon/MPhil-Code>

## References

- Aird, J., Coil, A. L., Georgakakis, A., et al. 2015, Monthly Notices of the Royal Astronomical Society, 451, 1892, doi: [10.1093/mnras/stv1062](https://doi.org/10.1093/mnras/stv1062)
- Alexander, D. M., & Hickox, R. C. 2012, New Astronomy Reviews, 56, 93, doi: [10.1016/j.newar.2011.11.003](https://doi.org/10.1016/j.newar.2011.11.003)
- Alqasim, A., & Page, M. J. 2023, Monthly Notices of the Royal Astronomical Society, 520, 3827, doi: [10.1093/mnras/stad007](https://doi.org/10.1093/mnras/stad007)
- Assef, R. J., Kochanek, C. S., Ashby, M. L. N., et al. 2011, The Astrophysical Journal, 728, 56, doi: [10.1088/0004-637X/728/1/56](https://doi.org/10.1088/0004-637X/728/1/56)
- Astropy Collaboration, Price-Whelan, A. M., Lim, P. L., et al. 2022, The Astrophysical Journal, 935, 167, doi: [10.3847/1538-4357/ac7c74](https://doi.org/10.3847/1538-4357/ac7c74)
- Benson, A. J., Bower, R. G., Frenk, C. S., et al. 2003, The Astrophysical Journal, 599, 38, doi: [10.1086/379160](https://doi.org/10.1086/379160)
- Binggeli, B., Sandage, A., & Tammann, G. A. 1988, Annual Review of Astronomy and Astrophysics, 26, 509, doi: [10.1146/annurev.aa.26.090188.002453](https://doi.org/10.1146/annurev.aa.26.090188.002453)
- Boquien, M., Burgarella, D., Roehlly, Y., et al. 2019, Astronomy and Astrophysics, 622, A103, doi: [10.1051/0004-6361/201834156](https://doi.org/10.1051/0004-6361/201834156)
- Brammer, G. B., van Dokkum, P. G., & Coppi, P. 2008, The Astrophysical Journal, 686, 1503, doi: [10.1086/591786](https://doi.org/10.1086/591786)
- Brown, A., Nayyeri, H., Cooray, A., et al. 2019, The Astrophysical Journal, 871, 87, doi: [10.3847/1538-4357/aaf73b](https://doi.org/10.3847/1538-4357/aaf73b)
- Bruzual, G., & Charlot, S. 2003, Monthly Notices of the Royal Astronomical Society, Volume 344, Issue 4, pp. 1000-1028., 344, 1000, doi: [10.1046/j.1365-8711.2003.06897.x](https://doi.org/10.1046/j.1365-8711.2003.06897.x)
- Burgarella, D., Buat, V., & Iglesias-Páramo, J. 2005, Monthly Notices of the Royal Astronomical Society, 360, 1413, doi: [10.1111/j.1365-2966.2005.09131.x](https://doi.org/10.1111/j.1365-2966.2005.09131.x)
- Calzetti, D., Armus, L., Bohlin, R. C., et al. 2000, The Astrophysical Journal, 533, 682, doi: [10.1086/308692](https://doi.org/10.1086/308692)
- Caputi, K. I., Lagache, G., Yan, L., et al. 2007, The Astrophysical Journal, 660, 97, doi: [10.1086/512667](https://doi.org/10.1086/512667)
- Chabrier, G. 2003, The Publications of the Astronomical Society of the Pacific, Volume 115, Issue 809, pp. 763-795., 115, 763, doi: [10.1086/376392](https://doi.org/10.1086/376392)
- Cicone, C., Maiolino, R., Sturm, E., et al. 2014, Astronomy and Astrophysics, 562, A21, doi: [10.1051/0004-6361/201322464](https://doi.org/10.1051/0004-6361/201322464)
- Cool, R. J., Eisenstein, D. J., Kochanek, C. S., et al. 2012, The Astrophysical Journal, 748, 10, doi: [10.1088/0004-637X/748/1/10](https://doi.org/10.1088/0004-637X/748/1/10)
- Cowley, M. J., Spitler, L. R., Tran, K.-V. H., et al. 2016, Monthly Notices of the Royal Astronomical Society, 457, 629, doi: [10.1093/mnras/stv2992](https://doi.org/10.1093/mnras/stv2992)
- Cowley, M. J., Spitler, L. R., Quadri, R. F., et al. 2018, Monthly Notices of the Royal Astronomical Society, 473, 3710, doi: [10.1093/mnras/stx2587](https://doi.org/10.1093/mnras/stx2587)
- Dai, X., Assef, R. J., Kochanek, C. S., et al. 2009, The Astrophysical Journal, 697, 506, doi: [10.1088/0004-637X/697/1/506](https://doi.org/10.1088/0004-637X/697/1/506)
- Dale, D. A., Helou, G., Magdis, G. E., et al. 2014, The Astrophysical Journal, 784, 83, doi: [10.1088/0004-637X/784/1/83](https://doi.org/10.1088/0004-637X/784/1/83)
- Delvecchio, I., Gruppioni, C., Pozzi, F., et al. 2014, Monthly Notices of the Royal Astronomical Society, 439, 2736, doi: [10.1093/mnras/stu130](https://doi.org/10.1093/mnras/stu130)
- Event Horizon Telescope Collaboration, Akiyama, K., Alberdi, A., et al. 2022, The Astrophysical Journal, 930, L12, doi: [10.3847/2041-8213/ac6674](https://doi.org/10.3847/2041-8213/ac6674)
- Finkelstein, S. L., & Bagley, M. B. 2022, The Astrophysical Journal, 938, 25, doi: [10.3847/1538-4357/ac89eb](https://doi.org/10.3847/1538-4357/ac89eb)
- Fiore, F., Feruglio, C., Shankar, F., et al. 2017, Astronomy and Astrophysics, 601, A143, doi: [10.1051/0004-6361/201629478](https://doi.org/10.1051/0004-6361/201629478)
- Fotopoulou, S., Buchner, J., Georgantopoulos, I., et al. 2016, Astronomy and Astrophysics, 587, A142, doi: [10.1051/0004-6361/201424763](https://doi.org/10.1051/0004-6361/201424763)
- Fu, H., Yan, L., Scoville, N. Z., et al. 2010, The Astrophysical Journal, 722, 653, doi: [10.1088/0004-637X/722/1/653](https://doi.org/10.1088/0004-637X/722/1/653)
- Giacconi, R., Zirm, A., Wang, J., et al. 2002, The Astrophysical Journal Supplement Series, 139, 369, doi: [10.1086/338927](https://doi.org/10.1086/338927)
- Grazian, A., Fontana, A., Santini, P., et al. 2015, Astronomy and Astrophysics, 575, A96, doi: [10.1051/0004-6361/201424750](https://doi.org/10.1051/0004-6361/201424750)
- Gruppioni, C., Pozzi, F., Zamorani, G., & Vignali, C. 2011, Monthly Notices of the Royal Astronomical Society, 416, 70, doi: [10.1111/j.1365-2966.2011.19006.x](https://doi.org/10.1111/j.1365-2966.2011.19006.x)
- Gruppioni, C., Pozzi, F., Rodighiero, G., et al. 2013, Monthly Notices of the Royal Astronomical Society, 432, 23, doi: [10.1093/mnras/stt308](https://doi.org/10.1093/mnras/stt308)
- Han, Y., Dai, B., Wang, B., Zhang, F., & Han, Z. 2012, Monthly Notices of the Royal Astronomical Society, 423, 464, doi: [10.1111/j.1365-2966.2012.20890.x](https://doi.org/10.1111/j.1365-2966.2012.20890.x)
- Harris, C. R., Millman, K. J., van der Walt, S. J., et al. 2020, Nature, 585, 357, doi: [10.1038/s41586-020-2649-2](https://doi.org/10.1038/s41586-020-2649-2)
- Hernán-Caballero, A., Alonso-Herrero, A., Hatziminaoglou, E., et al. 2015, The Astrophysical Journal, 803, 109, doi: [10.1088/0004-637X/803/2/109](https://doi.org/10.1088/0004-637X/803/2/109)
- Ho, L. C. 1999, The Astrophysical Journal, 516, 672, doi: [10.1086/307137](https://doi.org/10.1086/307137)
- Hopkins, P. F., Hernquist, L., Cox, T. J., & Kereš, D. 2008, The Astrophysical Journal Supplement Series, 175, 356, doi: [10.1086/524362](https://doi.org/10.1086/524362)
- Hopkins, P. F., & Quataert, E. 2010, Monthly Notices of the Royal Astronomical Society, 407, 1529, doi: [10.1111/j.1365-2966.2010.17064.x](https://doi.org/10.1111/j.1365-2966.2010.17064.x)
- Hopkins, P. F., Richards, G. T., & Hernquist, L. 2007, The Astrophysical Journal, 654, 731, doi: [10.1086/509629](https://doi.org/10.1086/509629)

- Huang, J. S., Ashby, M. L. N., Barmby, P., et al. 2007, *The Astrophysical Journal*, 664, 840, doi: [10.1086/519241](https://doi.org/10.1086/519241)
- Inoue, A. K. 2011, *Monthly Notices of the Royal Astronomical Society*, Volume 415, Issue 3, pp. 2920-2931., 415, 2920, doi: [10.1111/j.1365-2966.2011.18906.x](https://doi.org/10.1111/j.1365-2966.2011.18906.x)
- Katsianis, A., Blanc, G., Lagos, C. P., et al. 2017, *Monthly Notices of the Royal Astronomical Society*, 472, 919, doi: [10.1093/mnras/stx2020](https://doi.org/10.1093/mnras/stx2020)
- Kauffmann, G., Heckman, T. M., Tremonti, C., et al. 2003, *Monthly Notices of the Royal Astronomical Society*, 346, 1055, doi: [10.1111/j.1365-2966.2003.07154.x](https://doi.org/10.1111/j.1365-2966.2003.07154.x)
- Kennicutt, Jr., R. C. 1998, *The Astrophysical Journal*, 498, 541, doi: [10.1086/305588](https://doi.org/10.1086/305588)
- Kriek, M., van Dokkum, P. G., Labbé, I., et al. 2009, *The Astrophysical Journal*, 700, 221, doi: [10.1088/0004-637X/700/1/221](https://doi.org/10.1088/0004-637X/700/1/221)
- Lacy, M., Storrie-Lombardi, L. J., Sajina, A., et al. 2004, *The Astrophysical Journal Supplement Series*, 154, 166, doi: [10.1086/422816](https://doi.org/10.1086/422816)
- Lawrence, A., Warren, S. J., Almaini, O., et al. 2007, *Monthly Notices of the Royal Astronomical Society*, 379, 1599, doi: [10.1111/j.1365-2966.2007.12040.x](https://doi.org/10.1111/j.1365-2966.2007.12040.x)
- Leja, J., Johnson, B. D., Conroy, C., van Dokkum, P. G., & Byler, N. 2017, *The Astrophysical Journal*, 837, 170, doi: [10.3847/1538-4357/aa5ffe](https://doi.org/10.3847/1538-4357/aa5ffe)
- Lutz, D. 2014, *Annual Review of Astronomy and Astrophysics*, 52, 373, doi: [10.1146/annurev-astro-081913-035953](https://doi.org/10.1146/annurev-astro-081913-035953)
- Madau, P., & Dickinson, M. 2014, *Annual Review of Astronomy and Astrophysics*, 52, 415, doi: [10.1146/annurev-astro-081811-125615](https://doi.org/10.1146/annurev-astro-081811-125615)
- Magnelli, B., Popesso, P., Berta, S., et al. 2013, *Astronomy and Astrophysics*, 553, A132, doi: [10.1051/0004-6361/201321371](https://doi.org/10.1051/0004-6361/201321371)
- Merloni, A., & Heinz, S. 2008, *Monthly Notices of the Royal Astronomical Society*, 388, 1011, doi: [10.1111/j.1365-2966.2008.13472.x](https://doi.org/10.1111/j.1365-2966.2008.13472.x)
- Noll, S., Burgarella, D., Giovannoli, E., et al. 2009, *Astronomy and Astrophysics*, 507, 1793, doi: [10.1051/0004-6361/200912497](https://doi.org/10.1051/0004-6361/200912497)
- O'Connor, J. A., Rosenberg, J. L., Satyapal, S., & Secrest, N. J. 2016, *Monthly Notices of the Royal Astronomical Society*, 463, 811, doi: [10.1093/mnras/stw1976](https://doi.org/10.1093/mnras/stw1976)
- Page, M. J., Dwelly, T., McHardy, I., et al. 2021, *Monthly Notices of the Royal Astronomical Society*, 506, 473, doi: [10.1093/mnras/stab1638](https://doi.org/10.1093/mnras/stab1638)
- Persson, S. E., Murphy, D. C., Smee, S., et al. 2013, *Publications of the Astronomical Society of the Pacific*, 125, 654, doi: [10.1086/671164](https://doi.org/10.1086/671164)
- Pouliasis, E., Mountrichas, G., Georgantopoulos, I., et al. 2020, *Monthly Notices of the Royal Astronomical Society*, 495, 1853, doi: [10.1093/mnras/staa1263](https://doi.org/10.1093/mnras/staa1263)
- Rees, G. A., Spitler, L. R., Norris, R. P., et al. 2016, *Monthly Notices of the Royal Astronomical Society*, 455, 2731, doi: [10.1093/mnras/stv2468](https://doi.org/10.1093/mnras/stv2468)
- Robotham, A. S. G., Bellstedt, S., Lagos, C. d. P., et al. 2020, *Monthly Notices of the Royal Astronomical Society*, 495, 905, doi: [10.1093/mnras/staa1116](https://doi.org/10.1093/mnras/staa1116)
- Rodighiero, G., Vaccari, M., Franceschini, A., et al. 2010, *Astronomy and Astrophysics*, 515, A8, doi: [10.1051/0004-6361/200912058](https://doi.org/10.1051/0004-6361/200912058)
- Sanders, D. B., Mazzarella, J. M., Kim, D. C., Surace, J. A., & Soifer, B. T. 2003, *The Astronomical Journal*, 126, 1607, doi: [10.1086/376841](https://doi.org/10.1086/376841)
- Saunders, W., Rowan-Robinson, M., Lawrence, A., et al. 1990, *Monthly Notices of the Royal Astronomical Society*, 242, 318, doi: [10.1093/mnras/242.3.318](https://doi.org/10.1093/mnras/242.3.318)
- Schawinski, K., Thomas, D., Sarzi, M., et al. 2007, *Monthly Notices of the Royal Astronomical Society*, 382, 1415, doi: [10.1111/j.1365-2966.2007.12487.x](https://doi.org/10.1111/j.1365-2966.2007.12487.x)
- Schechter, P. 1976, *The Astrophysical Journal*, 203, 297, doi: [10.1086/154079](https://doi.org/10.1086/154079)
- Schmidt, M. 1968, *The Astrophysical Journal*, 151, 393, doi: [10.1086/149446](https://doi.org/10.1086/149446)
- Scoville, N., Aussel, H., Brusa, M., et al. 2007, *The Astrophysical Journal Supplement Series*, 172, 1, doi: [10.1086/516585](https://doi.org/10.1086/516585)
- Silk, J. 2013, *The Astrophysical Journal*, 772, 112, doi: [10.1088/0004-637X/772/2/112](https://doi.org/10.1088/0004-637X/772/2/112)
- Silva, L., Schurer, A., Granato, G. L., et al. 2011, *Monthly Notices of the Royal Astronomical Society*, 410, 2043, doi: [10.1111/j.1365-2966.2010.17580.x](https://doi.org/10.1111/j.1365-2966.2010.17580.x)
- Spitler, L. R., Labbé, I., Glazebrook, K., et al. 2012, *The Astrophysical Journal*, 748, L21, doi: [10.1088/2041-8205/748/2/L21](https://doi.org/10.1088/2041-8205/748/2/L21)
- Stalevski, M., Fritz, J., Baes, M., Nakos, T., & Popovic, L. C. 2012, *Monthly Notices of the Royal Astronomical Society*, Volume 420, Issue 4, pp. 2756-2772., 420, 2756, doi: [10.1111/j.1365-2966.2011.19775.x](https://doi.org/10.1111/j.1365-2966.2011.19775.x)
- Stalevski, M., Ricci, C., Ueda, Y., et al. 2016, *Monthly Notices of the Royal Astronomical Society*, 458, 2288, doi: [10.1093/mnras/stw444](https://doi.org/10.1093/mnras/stw444)
- Straatman, C. M. S., Spitler, L. R., Quadri, R. F., et al. 2016, *The Astrophysical Journal*, 830, 51, doi: [10.3847/0004-637X/830/1/51](https://doi.org/10.3847/0004-637X/830/1/51)
- Symeonidis, M., & Page, M. J. 2019, *Monthly Notices of the Royal Astronomical Society*, 485, L11, doi: [10.1093/mnras/slz022](https://doi.org/10.1093/mnras/slz022)
- . 2021, *Monthly Notices of the Royal Astronomical Society*, 503, 3992, doi: [10.1093/mnras/stab598](https://doi.org/10.1093/mnras/stab598)
- Szokoly, G. P., Bergeron, J., Hasinger, G., et al. 2004, *The Astrophysical Journal Supplement Series*, 155, 271, doi: [10.1086/424707](https://doi.org/10.1086/424707)
- Tempel, E. 2011, *Baltic Astronomy*, 20, 241, doi: [10.1515/astro-2017-0288](https://doi.org/10.1515/astro-2017-0288)
- Thorne, J. E., Robotham, A. S. G., Davies, L. J. M., et al. 2022, *Monthly Notices of the Royal Astronomical Society*, 509, 4940, doi: [10.1093/mnras/stab3208](https://doi.org/10.1093/mnras/stab3208)
- Toba, Y., Oyabu, S., Matsuhara, H., et al. 2013, *Publications of the Astronomical Society of Japan*, 65, 113, doi: [10.1093/pasj/65.5.113](https://doi.org/10.1093/pasj/65.5.113)
- Virtanen, P., Gommers, R., Oliphant, T. E., et al. 2020, *Nature Methods*, 17, 261, doi: [10.1038/s41592-019-0686-2](https://doi.org/10.1038/s41592-019-0686-2)
- Wu, Y., Shi, Y., Helou, G., et al. 2011, *The Astrophysical Journal*, 734, 40, doi: [10.1088/0004-637X/734/1/40](https://doi.org/10.1088/0004-637X/734/1/40)
- Wuyts, S., Labbé, I., Förster Schreiber, N. M., et al. 2008, *The Astrophysical Journal*, 682, 985, doi: [10.1086/588749](https://doi.org/10.1086/588749)
- Wylezalek, D., Vernet, J., De Breuck, C., et al. 2014, *The Astrophysical Journal*, 786, 17, doi: [10.1088/0004-637X/786/1/17](https://doi.org/10.1088/0004-637X/786/1/17)
- Yuan, Z., Wang, J., Worrall, D. M., Zhang, B.-B., & Mao, J. 2018, *The Astrophysical Journal Supplement Series*, 239, 33, doi: [10.3847/1538-4365/aacd3b](https://doi.org/10.3847/1538-4365/aacd3b)